A&A 570, A69 (2014)
DOI: 10.1051/0004-6361/201424419

Astronomy & Astrophysics

The GALEX Ultraviolet Virgo Cluster Survey (GUViCS)

IV. The role of the cluster environment on galaxy evolution⋆,⋆⋆

A. Boselli[1], E. Voyer[1], S. Boissier[1,2], O. Cucciati[3,2], G. Consolandi[4], L. Cortese[5], M. Fumagalli[6,9], G. Gavazzi[4], S. Heinis[7], Y. Roehlly[1], and E. Toloba[8,9]

[1] Aix-Marseille Université, CNRS, LAM (Laboratoire d'Astrophysique de Marseille), UMR 7326, 13388 Marseille, France
e-mail: Alessandro.Boselli@lam.fr
[2] I.N.A.F., Osservatorio Astronomico di Bologna, via Ranzani 1, 40127 Bologna, Italy
[3] Università di Bologna, Dipartimento di Fisica e Astronomia, viale Berti Pichat 6/2, 40127 Bologna, Italy
[4] Università di Milano-Bicocca, piazza della Scienza 3, 20100 Milano, Italy
[5] Centre for Astrophysics & Supercomputing, Swinburne University of Technology, Mail H30, PO Box 218, Hawthorn, VIC 3122, Australia
[6] Institute for Computational Cosmology, Department of Physics, Durham University, South Road, Durham DH1 3LE, UK
[7] Department of Astronomy, University of Maryland, College Park, MD 20742-2421, USA
[8] UCO/Lick Observatory, University of California, Santa Cruz, 1156 High Street, Santa Cruz, CA 95064, USA
[9] Carnegie Observatories, 813 Santa Barbara Street, Pasadena, CA 91101, USA

Received 17 June 2014 / Accepted 18 July 2014

ABSTRACT

We study the role of the environment on galaxy evolution using a sample of 868 galaxies in the Virgo cluster and in its surrounding regions that are selected from the GALEX Ultraviolet Virgo Cluster Survey (GUViCS) with the purpose of understanding the origin of the red sequence in dense environments. The sample spans a wide range in morphological types (from dwarf ellipticals to Im and BCD) and stellar masses ($10^7 \lesssim M_{\rm star} \lesssim 10^{11.5}\ M_\odot$). We collected multifrequency data covering the whole electromagnetic spectrum for most of the galaxies, including UV, optical, mid- and far-infrared imaging data, as well as optical and HI spectroscopic data. We first identify the different dynamical substructures that compose the Virgo cluster, and we calculate the local density of galaxies using different methods. We then study the distribution of galaxies belonging to the red sequence, the green valley, and the blue cloud within the different cluster substructures or as a function of galaxy density. Our analysis indicates that all the most massive galaxies ($M_{\rm star} \gtrsim 10^{11}\ M_\odot$) are slow rotators and are the dominant galaxies of the different cluster substructures, which are generally associated with a diffuse X-ray emission. They are probably the result of major merging events that occurred at early epochs, as also indicated by their very old stellar populations. Slow rotators of lower stellar mass ($10^{8.5} \lesssim M_{\rm star} \lesssim 10^{11}\ M_\odot$) are also preferentially located within the different high-density substructures of the cluster. Their position in the velocity space indicates that they are virialised within the cluster; thus, they are Virgo members since its formation. They have been shaped by gravitational perturbations occurring within the infalling groups that later form the cluster (pre-processing). On the contrary, low-mass star-forming systems are extremely rare in the inner regions of the Virgo cluster A, where the density of the intergalactic medium is at its maximum. Our ram pressure stripping models consistently indicate that these star-forming systems can be rapidly deprived of their interstellar medium during their interaction with the intergalactic medium. The lack of gas quenches their star-formation activity transforming them into quiescent dwarf ellipticals. This mild transformation does not perturb the kinematic properties of these galaxies, which still have rotation curves typical of star-forming systems.

Key words. galaxies: clusters: general – galaxies: clusters: individual: Virgo – galaxies: evolution – galaxies: interactions – galaxies: ISM – galaxies: star formation

1. Introduction

Multifrequency observations of nearby and high-redshift galaxies consistently indicate that mass is the principal driver of galaxy evolution (down-sizing effect; Cowie et al. 1996; Gavazzi et al. 1996; Boselli et al. 2001; Fontanot et al. 2009). Massive galaxies have formed most of their stars at early epochs, while dwarf systems are still active at a rate comparable to their mean star-formation rate during all their life. Observations, however, clearly indicate that mass is not the only parameter driving galaxy evolution. There is indeed strong observational evidence suggesting that the environment in which galaxies reside might be another key parameter. Since the seminal work of Dressler, we know that galaxies in high-density environments

⋆ Appendices are available in electronic form at http://www.aanda.org
⋆⋆ Full Table A.1 is only available at the CDS via anonymous ftp to cdsarc.u-strasbg.fr (130.79.128.5) or via http://cdsarc.u-strasbg.fr/viz-bin/qcat?J/A+A/570/A69

are preferentially ellipticals and lenticulars with the former dominating the core of rich clusters (morphology segregation effect; Dressler et al. 1980, 1997; Whitmore et al. 1993). There is also evidence that field galaxies, mainly late-type gas-rich systems, are falling into high-density regions (Colless & Dunn 1996; Rines et al. 2003). What is the fate of these freshly infalling systems in high density environments?

Clusters of galaxies are high-density environments characterised by a deep potential well trapping a hot and dense intergalactic medium emitting in the X-rays. The gravitational interactions of galaxies with other cluster members or with the potential of the cluster as a whole, as well as their interactions with the diffuse intergalactic medium, can easily remove their interstellar medium quenching their star-formation activity because of the lack of fresh fuel. Spiral galaxies can thus be transformed into quiescent systems (e.g. Boselli & Gavazzi 2006). While the main lines of this evolutionary picture through cosmic time are well understood (Elbaz et al. 2007; Bundy et al. 2010), we still do not know the exact contribution of each perturbing process since the formation of galaxies to the present epoch. Indeed, we still do not know which are the physical processes that gave birth to the different galaxy populations that inhabit rich clusters: massive and dwarf ellipticals, lenticulars and anemic spirals. We also do not know how the relative weight of the different processes that shape galaxy evolution changed since their formation. This is indeed expected given that the physical conditions characterising high-density regions (total mass, velocity dispersion, and density of the intergalactic medium) significantly changed with cosmic time.

The Virgo cluster is the highest density region close to the Milky Way. It is a cluster still in formation that is composed of different substructures similar to those expected in high redshift clusters. These substructures are quite different from one another, since they span a wide range in velocity dispersion, galaxy composition, and properties of the intergalactic medium. Virgo is thus an ideal laboratory for studying and comparing the effects induced by different kinds of perturbations. Furthermore, thanks to its proximity (~16.5–17 Mpc; Gavazzi et al. 1999; Mei et al. 2007), observations of Virgo dwarf galaxies are possible at almost any frequency. This is important, since these are the most fragile objects easily perturbed in any kind of physical process. At the same time, the angular dimension of galaxies is large enough to allow the detailed comparison of their radial properties with the prediction of different models of galaxy evolution. This is of paramount importance for the identification of the ongoing perturbing process (e.g. Boselli et al. 2006).

For all these reasons, the Virgo cluster has always been one of the preferred targets in environmental studies. After the seminal work of Binggeli, Sandage, and Tammann, (e.g. Binggeli et al. 1985), who mapped the whole cluster region in one optical band using photographic plates, however, blind surveys of the Virgo cluster were not possible up to the last years because of its large extension on the sky (more than 100 deg^2). Dedicated studies were, thus, focused on selected samples of galaxies for which multifrequency data were becoming available. It is only in the recent years that the advent of large panoramic detectors allowed the full mapping of the Virgo cluster in several photometric and spectroscopic bands. Multifrequency observations are crucial, since they provide information on the different components of galaxies, including both the young and old stellar populations, the different constituents of the interstellar medium (ISM; atomic and molecular gas, dust, metals), magnetic fields etc. They are thus a unique tool to study how the matter cycle in galaxies is perturbed in high-density environments (e.g. Boselli 2011). Several blind surveys of the Virgo cluster have been recently completed in the optical bands (NGVS; Ferrarese et al. 2012), the mid- (WISE; Wright et al. 2010) and far-infrared (HeViCS; Davies et al. 2010, 2012), and the 21 cm HI line (ALFALFA; Giovanelli et al. 2005). The GALEX Ultraviolet Virgo Cluster Survey (GUViCS; Boselli et al. 2011), a deep blind survey in two UV photometric bands of ~300 deg^2, which is centred on M87, has been recently completed. The UV data are sensitive to the emission of the youngest stars in star-forming systems (e.g. Kennicutt 1998a; Boselli et al. 2009) and to that of the most evolved stars in old, early-type galaxies (O'Connell 1999; Boselli et al. 2005). They are thus crucial for reconstructing the recent and past star-formation history of perturbed and unperturbed objects in the nearby universe.

It is thus time to revisit the seminal work of Sandage and collaborators and to extend the study of the Virgo cluster by taking benefit of the unique set of multifrequency photometric and spectroscopic data that is now available to the community. In this paper, we analyse the statistical properties of a large sample of more than eight hundred galaxies located in the Virgo cluster and in its surroundings. The effectiveness of using a statistical analysis based on multifrequency data in the study of the role of the environment on galaxy evolution has been recently shown in the works of Gavazzi et al. (2013a,b), which combined HI, Hα, and optical data in the Local supercluster, including Virgo, and in the Coma supercluster region. More recently, Cybulski et al. (2014) combined near- and mid-infrared data from the WISE survey (Wright et al. 2010) with UV data from GALEX to study the star formation-history of galaxies in the Coma supercluster region. Here we combine the new set of UV data from GALEX recently published in Voyer et al. (2014) with SDSS optical data, mid- and far-infrared data from WISE and *Herschel*, and HI data from ALFALFA to have a complete picture of galaxy evolution within the Virgo cluster region. Additionally, we add a few high-resolution spectroscopic data that are extremely useful in quantitatively estimating the kinematic properties of a representative subsample of massive and intermediate mass early-type systems. The results of this analysis are compared to the predictions of multizone chemo-spectrophotometric models of galaxy evolution presented in Boselli et al. (2006, 2008a), which are specially tailored to take two different processes induced by the cluster environment on galaxies into account: ram pressure stripping (Gunn & Gott 1972) and starvation (Larson et al. 1980). The study of the origin of the red sequence through the transformation of late-type galaxies in high-density environments has been the topic of several recent papers (e.g. Boselli et al. 2008a; Hughes & Cortese 2009; Cortese & Hughes 2009; Gavazzi et al. 2010, 2013a,b). At the same time the novelty of this work is that of using the largest sample with a complete set of multifrequency data that spans the whole electromagnetic spectrum, of extending previous analyses down to dwarf galaxies of stellar mass $M_{\rm star} \simeq 10^7\ M_\odot$, and of taking advantage of the proximity of Virgo to resolve galaxies within its cluster substructures where different physical processes are dominant.

The paper is structured as follows: in Sect. 2 we present the sample; in Sect. 3, the multifrequency set of data is used in the analysis, while we briefly describe our multizone chemo-spectrophotometric models of galaxy evolution in Sect. 4. In Sect. 5, we use the UV-to-optical colour magnitude relation to characterise the different galaxy populations, while we study the distribution of the different types of galaxies within the various substructures of the cluster in Sect. 6. The analysis is presented in Sect. 7, while a detailed discussion of the results is given in

Table 1. Completeness in the NUV band over the Virgo cluster region ($12h \leq RA \leq 13h$; $0° \leq Dec \leq 20°$).

Sample	Depth	Coverage	Completeness
AIS	~200 s	94%	20 mag
MIS	$\gtrsim$800 s	65%	21.5 mag

Sect. 8. In Appendix A, we present the new set of WISE data at 22 μm necessary to correct for dust attenuation the UV emission of the target galaxies, while we study how the use of standard recipes for determining the total stellar mass of galaxies might induce systematic effects in perturbed objects in Appendix B.

2. The sample

The sample analysed in this work has been extracted from the Extended Source Catalogue of Voyer et al. (2014), and it is composed of all galaxies detected by GALEX in the near-ultraviolet (NUV) band in the Virgo cluster region and its surroundings ($12h \leq RA \leq 13h$; $0° \leq Dec \leq 20°$) with a recessional velocity lower than 3500 km s^{-1}. The Extended Source Catalogue of Voyer et al. (2014) is composed of all galaxies listed in the Virgo Cluster Catalogue (VCC, Binggeli et al. 1985), the CGCG (Zwicky et al. 1961–1968), or other main catalogues (NGC, UGC, IC, DDO, KUG, FGC, MRK, LSBC, AGC, etc.) included in NED. The adopted threshold in redshift guarantees the inclusion of galaxies in the infalling regions and in the different substructures of Virgo that are mainly located at slightly higher distance than the main body of the cluster associated to M87, which is generally called cluster A (Gavazzi et al. 1999).

As defined, the analysed sample is optical and UV selected and can thus suffer from incompleteness in the two bands. In the optical band, the catalogues used to extract the target galaxies are not complete at the same depth over the studied region. The VCC, which covers the largest portion of the sky analysed in this work, is complete to the photographic magnitude $m_{pg} \simeq 18$. Down to this magnitude limit, the VCC is also almost complete in redshift (88%). Boselli et al. (2011) have shown that at the typical depth of the deep GUViCS observations (Medium Imaging Survey), 92% of the galaxies detected by GALEX with a NUV magnitude $\leq$21 mag have an optical counterpart in the VCC. At this depth, the GUViCS observations cover ~65% of the studied region and encompass the full VCC (Fig. 1). This region is slightly more extended than the virial radius of cluster A and B (the substructure associated to M49). In this region, the NUV catalogue is complete down to ~21.5 AB mag (Voyer et al. 2014). The same completeness in both the optical and UV bands is unfortunately not reached in the periphery of the cluster. The CGCG is complete to $m_{pg} \simeq 15.7$, while the other catalogues used to define the sample have been constructed using different selection criteria. In the same region, the sky coverage of GALEX at the depth of the MIS is also more sporadic. At the depth of the All sky Imaging Survey, the sample is complete only down to ~20 AB mag (see Table 1 and Fig. 1).

The final sample used in this work includes 868 objects down to the NUV limit of ~22 AB mag. The UV selection favors the detection of faint star-forming galaxies down to stellar masses $M_{star} \simeq 10^{6.5}\ M_\odot$ (see Sect. 3.2). Early-type galaxies, because of their quiescent nature, have redder colours than star-forming systems and are detected only to $M_{star} \simeq 10^7\ M_\odot$. The survey is complete to these stellar mass limits only at the depth of the MIS, thus, up to ~1 virial radius of cluster A and B, and within all the other cluster substructures (see Sect. 6.1). However, in the periphery of the cluster, where the NUV data comes principally from the AIS, the sample is only complete to $M_{star} \simeq 10^8$–$10^{8.5}\ M_\odot$ in quiescent objects with red colours.

3. The data

3.1. The multifrequency data

The Virgo cluster region has been the target of the GALEX Virgo Cluster Survey (GUViCS; Boselli et al. 2011). Because of the adopted selection criteria (see Sect. 2), all galaxies have GALEX data in the near-ultraviolet (NUV) band ($\lambda_{eff} = 2316$ Å, $\Delta\lambda = 1060$ Å), while only 531 (62%) are in the FUV-band ($\lambda_{eff} = 1539$ Å, $\Delta\lambda = 442$ Å) down to 22 AB mag. The UV data have been taken from the GUViCS catalogue that is recently published in Voyer et al. (2014). Being extended sources, the UV flux of galaxies at the distance of Virgo has been extracted by using ad hoc procedures defined to encompass their whole emission. The UV fluxes analysed in this work can thus be considered as total entities.

The UV data are combined with optical data to constrain the properties of the stellar emission within galaxies. The optical data have been taken in the SDSS photometric bands (u, g, r, i, z) from the SDSS (Abazajian et al. 2009). To avoid the use of the datasets extracted from the standard pipelines, which are known to suffer important shredding given the extended nature of these nearby galaxies as in the UV bands, optical magnitudes have been taken from imaging photometry for extended sources specially tuned to measure the total emission of these targets. These data come, in order of preference, from the SDSS imaging of the *Herschel* Reference Sample (Boselli et al. 2010) which has been recently published by Cortese et al. (2012a) and includes the brightest 172 objects, the compilation of Consolandi et al. (in prep.) that is determined by fitting composite radial light profiles for galaxies with stellar masses $M_{star} \gtrsim 10^{9.5}\ M_\odot$, the set of data determined using a similar procedure by Grossetti (2010) and Galardo (2010), aperture photometry (Gavazzi et al. 2013a), or the SDSS standard pipeline for the remaining faintest objects. Photometric optical data are available for all the galaxies of the sample. The SDSS also provides nuclear spectra (in a circular aperture of 3 arcsec) for 575 galaxies of the sample. These nuclear spectra are used to identify post-starburst galaxies (PSB or k+a) using the criterion described in Poggianti et al. (2004) and Dressler et al. (1999; see however Quintero et al. 2004). These are galaxies with a Balmer absorption line with an equivalent width $EW\mathrm{H}\delta > 3$ Å for a signal-to-noise larger than 5. They are also used to identify galaxies with a nuclear star formation, as those objects with a Balmer Hα emission line $EW\mathrm{H}\alpha > 3$ Å (with a signal-to-noise larger than 5). In bright galaxies, which are not fully sampled in the spectroscopic SDSS survey, this condition might include active galactic nuclei. For these reasons, this nuclear classification is used in the following analysis only for objects of low and intermediate stellar mass ($M_{star} \leq 10^{9.5}\ M_\odot$).

The determination of the dust attenuation in the different photometric bands, in particular in the UV ones, requires the use of infrared data (see below). To gather this information, we extract infrared data in the 22 μm band from the WISE survey (Wright et al. 2010). To avoid any possible systematic effect due to the extended nature of the target galaxies, we do not use published catalogues which are optimised for point-like sources but rather extract fluxes from the images using procedures similar to those adopted in the other bands, as described in Appendix A. The WISE detections at 22 μm are available for 407 objects (47%).

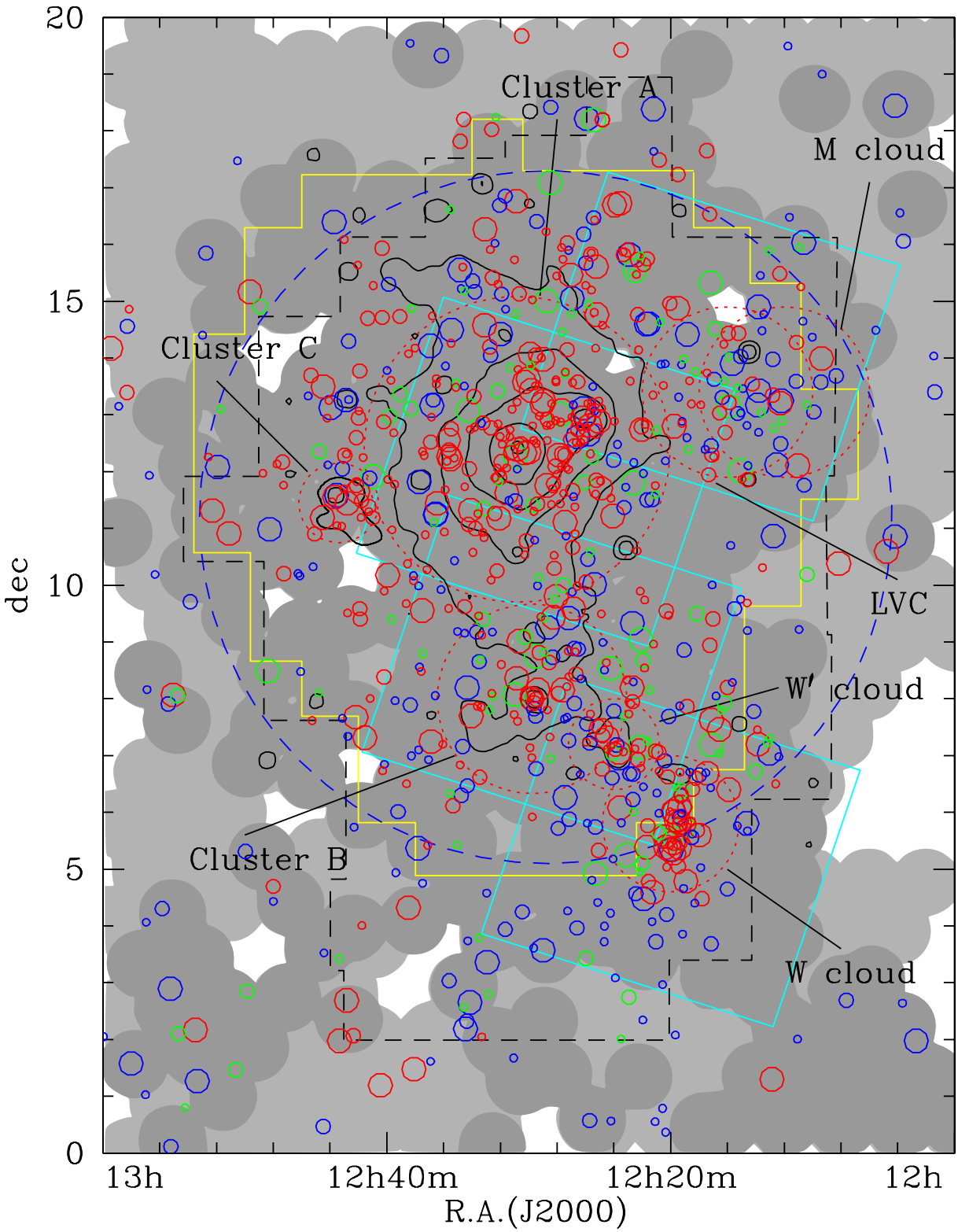

Fig. 1. Sky distribution of the GUViCS galaxies with a recessional velocity $vel \leq 3500$ km s^{-1}. Red, green, and blue symbols are for galaxies located in the red sequence, green valley, and blue cloud, respectively (see Sect. 5). The size of the symbols is proportional to the stellar mass of the galaxies: big symbols are for galaxies with $M_{\rm star} > 10^{9.5}$ $M_{\odot}$, medium symbols for objects with $10^{8.5} < M_{\rm star} \leq 10^{9.5}$ $M_{\odot}$, and small symbols for $M_{\rm star} \leq 10^{8.5}$ $M_{\odot}$. The red and blue dashed circles show the identified substructures used in the following analysis. The field is defined as composed by all the galaxies located outside the blue dashed circle and not belonging to any other structure. Light grey indicate shallow (exposure time <800 s) NUV GALEX fields; dark grey are deep fields (exposure time >800 s). The footprint of the VCC is shown by the black dashed line, NGVS by the yellow solid line, and HeViCS by the cyan solid line. The black contours indicate the X-ray diffuse emission of the cluster from Böhringer et al. (1994).

Table 2. Completeness of the sample in the different photometric bands.

Sample	*N*.	%
Full sample	868	100
FUV	537	62
NUV	868	100
SDSS(phot)	867	100
SDSS(spec)	575	67
WISE	868(407)	100(47)
Herschel	561(226)	65(26)
HI	742(354)	85(41)
Kinematic	111	13

Notes. The detected galaxies are in parenthesis.

The UV catalogue analysed in this work has also been cross-matched with the ALFALFA HI survey (Giovanelli et al. 2005) that is recently published in Haynes et al. (2011). Given the limited sensitivity of this survey (rms $\sim$ 2.3 mJy at 5 km s^{-1} spectral resolution), which allows the detection of galaxies with M(HI) $\simeq 10^{7.5}$ $M_\odot$ at the typical distance of Virgo, we also cross-matched the UV catalogue with deep HI data collected in the GOLDMine database (Gavazzi et al. 2003) that is available mainly for late-type galaxies, where the sensitivity is up to a factor of ~5 higher. The HI masses are available for 354 mainly late-type galaxies. Including upper limits, HI data are available for 742 objects.

To characterise the properties of the ISM of galaxies, our sample of UV selected objects has been also cross-matched with the catalogue of Auld et al. (2013), which is composed of VCC galaxies mapped with *Herschel* during the HeViCS survey (Davies et al. 2010). This survey does not cover the full sky region analysed in this work but is limited to the central ~84 deg^2 region of the cluster as depicted in Fig. 1. The survey, which is fairly complete down to ~100 mJy at 250 μm, observed 561 Virgo cluster members that are included in our sample and detected 226 of them[1].

Morphological types are taken from the VCC (Binggeli et al. 1985) or from its updated revisions (Binggeli et al. 1993). For galaxies outside the Virgo cluster, morphological types have been determined by us after the visual inspection of the SDSS images. As selected, all galaxies have also a redshift measurement necessary to guarantee their membership to the cluster. Kinematic data are available for a small subsample of galaxies. The ATLAS^{3D} spectroscopic survey (Cappellari et al. 2011a) provides a homogeneous estimate of the spin parameter measured within the effective radius λ_e for 74 bright galaxies (Emsellem et al. 2011), while similar data obtained from long slit spectroscopy are also available for 37 dwarf galaxies from the recent compilation of Toloba et al. (2011, 2014). Table 2 summarises the completeness of the sample in the different photometric bands.

In the following analysis, we compare the properties of the observed galaxies to those of the Virgo cluster itself that are locally determined using the X-ray emission of the hot diffuse gas. The properties of the emitting gas trapped within the potential well of the cluster are determined here using ROSAT data from Böhringer et al. (1994).

[1] To be conservative, we consider as detected galaxies only those with a signal-to-noise larger than 5 here.

3.2. The derived parameters

The multifrequency data in our hands allow us to determine several physical quantities useful for the following analysis. Distances are determined assuming the mean distance of the different cluster substructures indicated in Table 3, as suggested by Gavazzi et al. (1999). For galaxies at the periphery of the cluster, we assume the typical distance of the main body of the cluster (17 Mpc).

The UV and optical data are first corrected for dust attenuation. This is done using the prescription of Hao et al. (2011) based on the relation:

$$A(\mathrm{NUV})(\mathrm{mag}) = 2.5 \log \left[1 + 2.26 \frac{L(25\,\mu\mathrm{m})}{L(\mathrm{NUV})_{\mathrm{obs}}} \right], \quad (1)$$

where A(NUV) is the NUV attenuation (in mag) and $L(25\ \mu\mathrm{m})$ and $L(\mathrm{NUV})_{\mathrm{obs}}$ are the observed 25 μm and NUV luminosities (both expressed in erg s^{-1})[2], which assumes that the energy absorbed by dust is re-emitted in the far infrared domain. Given that dust might be heated also by the old stellar population in massive, quiescent late-type galaxies, the attenuation might be slightly overestimated in these systems (Hao et al. 2011). The WISE data are first multiplied by a factor 1.22, as indicated by Ciesla et al. (2014), to consider the systematic difference observed between the 22 μm WISE and the 24 μm MIPS bands, which are assumed to be representative of the 25 μm band. The internal attenuation in the other photometric bands from the FUV-to-the i-band is determined through the relation:

$$A(\lambda) = A(\mathrm{NUV}) \frac{k(\lambda)}{k(\mathrm{NUV})}, \quad (2)$$

where $k(\lambda)$ is the extinction coefficient determined from the Galactic extinction law of Fitzpatrick & Massa (2007). This determination of the attenuation in the other different bands is a rough estimate, since it considers that dust and stars of different ages are mixed in a slab model. A more sophisticated correction, such as the one proposed by Boselli et al. (2003a) that assumes that the ratio of the thickness of the dusty disc to the stellar disc changes with the mean age of the emitting stars and thus with the photometric band (sandwich model), is unfortunately impossible because we do not have a measurement of the correct inclination of all the galaxies. We notice, however, that the slab approximation is realistic for the UV bands, where the attenuation is at its maximum and is properly corrected using the prescription given in Eq. (2). Any systematic effects in the other bands should, however, be minor (~0.1 mag) when compared to the colour variations observed among the different galaxy populations (~3 mag). The correction for dust attenuation is applied only to late-type systems. The WISE data are available for most of the massive galaxies, while they are lacking for a significant fraction of the dwarf star-forming systems (see Appendix A). Given their low metallicity and dust content, we expect that dust attenuation in these objects is relatively low. We thus do not apply any correction in WISE undetected late-type systems.

Once corrected for attenuation, these data are used to estimate stellar masses. This is done using the prescription of Zibetti et al. (2009) based on the i-band luminosity combined with the $g-i$ colour index. Although this is a standard prescription generally used in the literature, we recall that it might give erroneous

[2] NUV data, as other photometric data in UV and optical bands, are first corrected for Galactic attenuation using the Schlegel et al. (1998) map combined with the Fitzpatrick & Massa (2007) extinction curve.

Table 3. Properties of the different cluster substructures (see Fig. 1).

Substructure	RA(J2000) °	Dec °	Radius °	Velocity range km s^{-1}	Dist[a] Mpc	$\langle vel \rangle$ km s^{-1}	σ km s^{-1}	N.	ρ^b N gal Mpc^{-3}	Central galaxy
Cluster A	187.71	12.39	<2.692[c]	<3500	17	955	799	234	110	M87
Cluster B	187.44	8.00	<1.667[c]	<3500	23	1134	464	66	53	M49
Cluster C	190.85	11.45	<0.7	<3500	17	1073	545	19	507	M60
W cloud	185.00	5.80	<1.2	$1000 < vel < 3500$	32	2176	416	66	52	NGC 4261
W′ cloud	186.00	7.20	<0.8	<2000	23	1019	416	28	202	NGC 4365
M cloud	183.00	13.40	<1.5	$1500 < vel < 3500$	32	2109	280	21	9	NGC 4168
LVC cloud	184.00	13.40	<1.5	$vel < 400$	17	85	208	21	57	NGC 4216
Field	187.20	11.20	>6.1	<3500	17	1537	635	138	0.05[d]	–

Notes. Galaxies in the overlapping regions that satisfy the membership criteria of two different structures are assumed to be members of the smallest structure. [(a)] Mean distance of each single substructure taken from Gavazzi et al. (1999). [(b)] Mean density assuming a spherical geometry of the substructure. [(c)] Radius corresponding to half of the virial radius from McLaughlin (1999) and Ferrarese et al. (2012). [(d)] The mean density at the periphery of the cluster is probably underestimated because there the GALEX observation are, on average, less deep than in the inner ~100 deg^2.

results in galaxies that recently truncated their star-formation activity on a very short timescale, such as those analysed in this work. We discuss any possible systematic effect in the determination of the stellar mass of galaxies that is related to environmental effects in Appendix B.

The ALFALFA and GOLDMine HI data are used to determine the HI-deficiency parameter, which is defined as the difference between the expected and the observed HI gas mass of each single galaxy on logarithmic scale (Haynes & Giovanelli 1984). The expected atomic gas mass is the mean HI mass of a galaxy of a given optical size and morphological type determined in a complete sample of isolated galaxies taken as reference. The HI-deficiency parameter has been measured only in late-type galaxies using the recent calibrations of Boselli & Gavazzi (2009). We consider those late-type galaxies with an HI-deficiency parameter $HI-def \leq 0.4$ as unperturbed objects.

Kinematic data are used to differentiate rotationally-supported from pressure-supported systems. This is done by means of the spin parameter λ defined as in Emsellem et al. (2011). Emsellem et al. (2011) have identified those objects where $\lambda_e > 0.31\sqrt{\epsilon}$ as fast rotators, where ϵ is the ellipticity of the galaxy[3].

4. The models

We compare the observational results to the predictions of models of galaxy evolution specially tailored to simulate the effects induced by the interaction of galaxies with the hostile cluster environment extensively described in Boselli et al. (2006, 2008a). The evolution of galaxies is traced using the multizone chemical and spectrophotometric models of Boissier & Prantzos (2000), which are updated with an empirically determined star-formation law (Boissier et al. 2003) relating the star-formation rate to the total gas surface densities. These models were shown to reproduce realistic multiwavelength profiles in comparison to those observed in SING galaxies (Munoz-Mateos et al. 2011). These models are modified to simulate two different effects induced by the interaction of galaxies with the hot intergalactic medium permeating the potential well of the cluster. In the starvation scenario (Larson et al. 1980; Balogh et al. 2000; Treu et al. 2003), the cluster acts on large scales by removing any extended gaseous halo surrounding the galaxy, preventing further infall of such gas onto the disk. The galaxy then becomes anemic simply because it exhausts the gas reservoir through ongoing star formation. Our unperturbed model galaxy does not have a hot halo gas. To reproduce its chemo-spectrophotometric radial gradients, however, the model requires the infall of pristine gas from the surrounding medium. This infall is rapid at early epochs in massive objects, while it is more gradual in time in low-mass systems (Boissier & Prantzos 2000; Munoz-Mateos et al. 2011). Starvation has been simulated just by stopping the infall of gas in the model. We recall that this definition is rather different than the one often adopted in cosmological simulations, where the hot halo gas is generally instantaneously removed once the galaxy enters the massive dark matter halo of the cluster (e.g. De Lucia 2011). In our model, starvation is a passive phenomenon, where the gas is only consumed via star formation.

The second simulated effect is the ram pressure exerted by the dense intracluster medium ($\rho \sim 2\times10^{-3}$ atoms cm^{-3}; Boselli & Gavazzi 2006) on galaxies crossing the cluster at high velocity (~1000 km s^{-1}, Gunn & Gott 1972). Gas removal induces a quenching of the star-formation activity, making galaxies redder[4]. The ram pressure stripping event is simulated by assuming a gas-loss rate inversely proportional to the potential of the galaxy with an efficiency depending on the IGM gas density radial profile of the Virgo cluster given by Vollmer et al. (2001).

Both starvation and ram pressure stripping models have been determined for galaxies with a spin parameter $\lambda = 0.05$, the typical value for normal late-type galaxies as those analysed in this work (Mo et al. 1998; Munoz-Mateos et al. 2011), and rotational velocities of 40, 55, 70, 100, 130, and 220 km s^{-1} to reproduce galaxies spanning a wide range in total mass. For the ram pressure model, we use the stripping efficiency $\epsilon_0 = 1.2\ M_\odot$ kpc^{-2} yr^{-1} that reproduces the radial profiles of the Virgo cluster galaxy NGC 4569 (Boselli et al. 2006). In Boselli et al. (2006, 2008a) we have shown how the physical properties of galaxies (gas content, star-formation rate, colours, etc.) change as a function of time and depend on the gas stripping efficiency. Although the effects strongly depend on the assumed value of ϵ_0, we have adopted the values suggested by these studies. We note that this calibration was made at the present epoch. The relative effect would be smaller at earlier epochs because of a lower density of the intracluster medium and a lower velocity dispersion within the younger cluster. However, multiple crossings of the

[3] With respect to the original classification of Emsellem et al. (2011), M60 is considered here as a slow rotator for the reasons given in Sect. 8.1.

[4] In a ram pressure stripping event, the infall of pristine gas is also stopped.

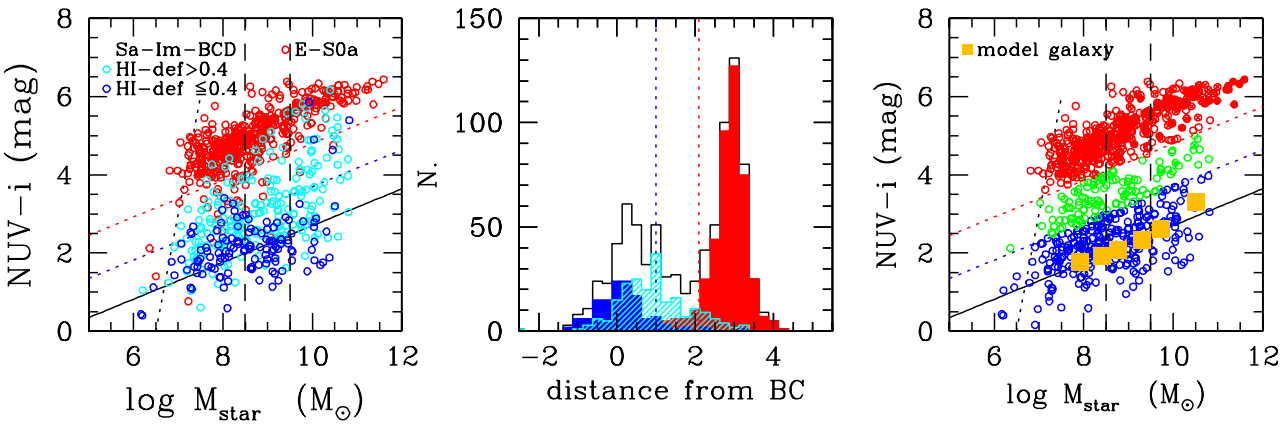

Fig. 2. *Left*: extinction corrected $NUV - i$ (AB system) vs. $M_{\rm star}$ relation for all galaxies of the sample. Red symbols are for early-type systems (dE-E-S0a); dark and light blue symbols are for gas normal ($HI - def \leq 0.4$) and gas-deficient ($HI - def > 0.4$) late-type galaxies (Sa-Im-BCD). The solid black line shows the typical $NUV - i$ vs. $M_{\rm star}$ relation for model unperturbed late-type galaxies. The black dotted vertical line shows the limit of the GUViCS survey, which is more efficient at detecting blue star-forming systems than red objects. The vertical dashed lines show the interval in stellar mass used to define massive, intermediate, and low-mass objects within the sample. The red and blue dotted lines indicate the limit used to define the red sequence and the blue cloud. *Centre*: distribution of the colour difference $(NUV - i) - (NUV - i)_{\rm Mod}$ (distance from the blue cloud BC) for the whole sample (black), for early-type galaxies (red), and for HI-normal ($HI - def \leq 0.4$; dark blue) and gas-deficient ($HI - def > 0.4$; light blue) late-type galaxies. The vertical red and blue dotted lines indicate the limits used to identify the red sequence and the blue cloud. *Right*: $NUV - i$ vs. $M_{\rm star}$ relation where galaxies are coded according to their belonging to the red sequence (red), green valley (green), and blue cloud (blue). The unpeturbed model galaxies are indicated by orange filled squares. Lines are as in the left panel.

cluster occuring at every ∼1.7 Gyr (Boselli & Gavazzi 2006) make the ram pressure stripping process more and more efficient to alter the galaxies properties as time passes (Boselli et al. 2008a). To mimic starvation, the infall is stopped at different epochs from the present to 9.7 Gyr ago (equivalent to $z \sim 1.6$). To quantify the effects induced by the cluster environments, all ram pressure stripping and starvation models are compared to those of unperturbed objects of a similar rotational velocity and spin parameter. These models of unperturbed galaxies are indicated as orange filled squares in the following figures.

5. The colour-stellar mass relation

The colour-stellar mass relation has been often used in the literature to identify galaxies at different stages of their evolution in various environments (Boselli et al. 2008a, 2014; Hughes & Cortese 2009; Cortese & Hughes 2009; Gavazzi et al. 2010, 2013a,b). This relation is indeed of paramount importance for comparison with models in the study of the formation of the red quiescent galaxy population dominating rich clusters (e.g. Boselli et al. 2008a). Figure 2 shows the $NUV - i$ vs. $M_{\rm star}$ relation for the observed galaxies. The $NUV - i$ colour index is sensitive to the relative weight of young stars emitting in the UV bands (Kennicutt 1998a; Boselli et al. 2001, 2009) and the bulk of the stellar population dominated by evolved stars in the optical i-band. It is thus a direct tracer of the mean age of the underlying stellar population that is very sensitive to abrupt variations of the star-formation activity, as those expected to affect cluster galaxies. In the left panel of Fig. 2, galaxies have different symbols according to their morphological classification, and, in late-type objects, to their HI gas content. It is evident that, as previously noticed by Hughes & Cortese (2009), Cortese & Hughes (2009), and Gavazzi et al. (2013a,b), gas-poor late-type galaxies have redder $NUV - i$ colours than unperturbed galaxies of similar stellar mass on average.

The $NUV - i$ colour-stellar mass relation has often been used to resolve the red sequence, which is composed of quiescent early-type systems, from the blue cloud of star-forming, late-type galaxies (Gil de Paz et al. 2007) and to identify galaxies in the region between these two sequences, which is generally called the green valley (e.g. Martin et al. 2007). Following Cortese & Hughes (2009), we use this diagram to separate galaxies in the three colour-stellar mass sequences. The red sequence can be easily identified and separated in the diagram using the relation $NUV - i = 0.47 \log M_{\rm star} + 0.1$[5]. The separation between the blue cloud and the green valley is less direct in this sample, which includes a large fraction of perturbed objects. To select galaxies in the three sequences, we first define the typical $NUV - i$ vs. $M_{\rm star}$ relation that is expected for field systems using our models of galaxy evolution for unperturbed objects ($(NUV - i)_{\rm Mod} = 0.47 \log M_{\rm star} - 2.0$). Curiously, the slope of the relation corresponds to that determined to separate the red sequence. To define the dynamic range in the $NUV - i$ colour typical of unperturbed blue cloud galaxies, we plot the distribution of the colour difference $(NUV - i) - (NUV - i)_{\rm Mod}$ in Fig. 2 or, in other words, the distance in colour from the blue cloud at a given stellar mass for HI-normal and HI-deficient ($HI - def \leq$ and >0.4) galaxies. Galaxies with an HI-deficiency parameter $HI - def \leq 0.4$ are taken here as representative of the typical unperturbed field population. Figure 2 clearly shows that the distribution in colour of the HI-normal late-type systems is symmetric and peaks around the $NUV - i$ vs. $M_{\rm star}$ relation which is drown by the unperturbed model galaxies. It drops to ≃0 at $(NUV - i) - (NUV - i)_{\rm Mod} = \pm 1$ mag, while that of HI-deficient cluster galaxies is, on average, redder. We, thus, define the limit between the blue cloud and the green valley with the relation $NUV - i = 0.47 \log M_{\rm star} - 1.0$. The slope of the $NUV - i$ vs. $M_{\rm star}$ relation described by the model galaxies used here to select objects that belong to the blue cloud is steeper than the one determined using different sets of data by Wyder et al. (2007) or Cortese et al. (2009). These definitions, as every definition

[5] This limit corresponds to a typical colour $\sim 1.5\sigma$ bluer than the median $(NUV - i) - (NUV - i)_{\rm Mod}$ colour of early-types, where σ is the typical dispersion of the red sequence.

of red sequence, green valley, and blue cloud galaxies, are still quite arbitrary. We recall, however, that we use these definitions to identify galaxies according to the mean age of their underlying stellar population and study their relative distribution within the cluster (centre vs. periphery; in the different substructures; as a function of galaxy density). Relative measurements, at least at the first order, are not sensitive to the adopted definitions of the three different sequences. Indeed, the main results of this work do not change whether different definitions are used.

6. The galaxy distribution within the cluster

6.1. Identification of the substructures on the plane of the sky

Once identified according to their spectrophotometric properties, we can use the complete coverage of the GUViCS survey to see how the different kinds of galaxies are distributed within the various known substructures composing the Virgo cluster and its surrounding regions. To do that, we plot the distribution on the plane of the sky of all the galaxies of the sample with different symbols to identify galaxies in the three colour sequences in three different bins of stellar mass in Fig. 1. We also plot the contours of the X-ray emitting gas showing the distribution of the hot and dense intracluster medium.

Thanks to the large number of galaxies with spectrophotometric data and spectroscopic information within the surveyed region, Fig. 1 can be used to identify the different substructures of the Virgo cluster, as originally defined by Binggeli et al. (1987, 1993). An overdensity of galaxies is indeed observed on the main peak of the X-ray emission of the cluster, which is centred on M87. This structure, which is the main structure of the whole cluster, is generally called Virgo cluster A. South of this region at RA $\sim$ 12h30m and Dec $\sim$ 8°, there is another condensation of galaxies associated with a second peak of the X-ray emission. This substructure is generally called Virgo cluster B, centred on the giant elliptical M49. A third peak of density is present east of Virgo cluster A at RA $\sim$ 12h45m and Dec $\sim$ 11.5°, which is again associated with a peak of X-ray emission and centred on the elliptical galaxy M60 (Virgo cluster C). There are three other obvious galaxy overdensity regions: one associated with a hot diffuse gas overdensity at RA 12h24m and Dec 7.2° (W′ cloud) and the other two at RA 12h20m and Dec 5.8° (W cloud) and RA 12h12m and Dec 13.4° (M cloud). East of the M cloud there is a second structure easily identifiable in the velocity space, which is generally called the low velocity cloud (LVC; Hoffman et al. 1989).

6.2. Identification of the substructures in the velocity space

These structures, which are characterised by different mean recessional velocities, are known to be at different distances (Binggeli et al. 1987, 1993; Gavazzi et al. 1999). We, thus, use velocity constraints, as indicated in Table 3, to assign the membership of galaxies to the different substructures, as originally done by de Vaucouleurs (1961), Ftaclas et al. (1984), Binggeli et al. (1987), and Hoffman et al. (1989). For the purpose of the present work, we identify as members of Virgo cluster A and B those galaxies with an angular distance that is smaller than half the virial radius of these two structures measured by McLaughlin (1999) and Ferrarese et al. (2012). The choice of half a virial radius is taken to avoid the uncertain identification of galaxies in possible overlapping regions in the two substructures. For the remaining substructures, we take arbitrary values for limiting the angular distance from the overdensity peak. This choice is

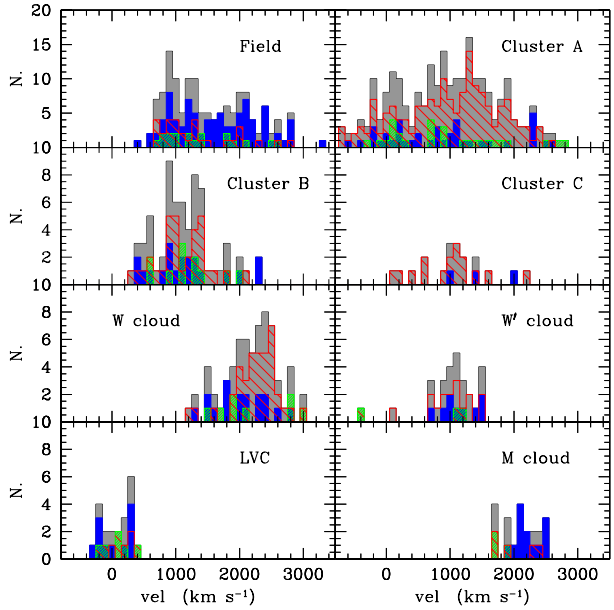

Fig. 3. Velocity distribution of galaxies within the different cluster substructures and in the field. The grey histogram shows the distribution of all galaxies; the red, green, and blue histograms are those objects belonging to the red sequence, the green valley, and the blue cloud, respectively.

dictated by the possibility that the identification of virial entities here using analytic prescriptions, such as the one proposed by Finn et al. (2005), might be not appropriate given the unrelaxed nature of these substructures. The resulting distribution of galaxies belonging to the different substructures in the velocity space is shown in Fig. 3.

Galaxies located outside a circular region centred at RA 12h29m and Dec 11.2° of radius 6.1 degrees (corresponding to ≃1.8 Mpc at the typical distance of Virgo which is assumed to be 17 Mpc) and not belonging to the other substructures are considered here as field objects and are used as reference samples in the following analysis. We recall, however, that these objects are not genuine field galaxies just because they are located at the periphery of the cluster. This limiting region, indeed, roughly corresponds to the virial radius of cluster A ($R_{\rm vir}(A) \simeq 1.6$ Mpc) and might thus be still affected by the cluster environment. Indeed, their velocity distribution peaks at ∼1000 km s^{-1}, which is the mean recessional velocity of cluster A.

6.3. Determination of the galaxy density

The data in our hand can be used to estimate the mean galaxy density around each single object. This exercise, however, is made difficult by the elongated 3D-structure of the cluster. Indeed, Virgo is composed of different substructures overlapping on the line of sight and located at different distances. Unfortunately, an accurate determination of the distance is available only for a small fraction of the targets. Given the large velocity dispersion within the cluster, the recessional velocity cannot be taken as a distance tracer through the Hubble relation. We thus decided to estimate mean surface densities rather than volume densities of galaxies. To do that, we cut the Virgo cluster region in the velocity space to separate galaxies belonging to the different substructures, as indicated in Table 3. We then apply two different methods to calculate the local density of galaxies around each object of the sample.

The first method consists of counting the number of galaxies within a cylinder of radius 0.2 Mpc (assuming the mean distance of each single substructure) centred on each single galaxy and with a depth corresponding to the velocity range indicated in Table 3. For simplicity, all "field" galaxies and galaxies that are not included in any of the regions, as indicated in Table 3 with a recessional velocity <3500 km s^{-1}, are assumed at 17 Mpc. This strong assumption probably induces an overestimate of the galaxy density in the periphery of the cluster, where a significant fraction of galaxies might be in Hubble flow. We recall, however, that all galaxies observed within the GUViCS survey with a recessional velocity <3500 km s^{-1} are located within ≃2 virial radii of cluster A and can thus be considered as Virgo members, as indicated by the velocity distribution shown in Fig. 3. The choice of such a small radius for the cylinder is dictated by the reason that we want to estimate density variations on relatively small scales comparable to those of the smallest substructures already identified in Virgo.

The second method is the Voronoi tessellation method. For each galaxy, we first define the Voronoi cells as the polygonal cells centred on the galaxy and enclosing all the surrounding empty space closest to that point. This method has proven to be very efficient in determining galaxy densities in different environments (Platen et al. 2011; Scoville et al. 2013; Cybulski et al. 2014) and in finding bound structures like galaxy groups (Marinoni et al. 2002; Gerke et al. 2005; Cucciati et al. 2010). The local density around the galaxy is then simply given by the inverse of the area of the Voronoi cell. To avoid projection effects, we adopt the same cut in the velocity space as those adopted for the cylinder method.

Both methods are only applied to those galaxies observed in deep observations (those located within the dark grey regions in Fig. 1) to avoid systematic effects in the density estimate. Indeed, in the outer regions, where the GALEX observations are shallower, the mean density might be underestimated just because the faintest galaxies are not detected. In the case of the cylinders, this is taken into account by dividing the local density around each galaxy by the fraction of the volume of the cylinder that falls within the area covered by the deep observation. This method has already been effectively used to correct for boundary effects (see e.g. Cucciati et al. 2006). In the case of the Voronoi tessellation, we did not try to correct for boundary effects given by the use of the deep data only. This might induce a possible underestimate of the local density for galaxies that reside in the Virgo outskirts. We decided not to correct the Voronoi local density because the Voronoi tessellation is an adaptive method that strongly depends on galaxy relative position, and it is harder to correct for boundary effects not knowing where the closest galaxy lies. Nevertheless, as explained below, we are more interested in contrasting low and high densities than determining the exact density value. Moreover, we find very similar results when using the density computed in cylinders and the one computed with the Voronoi tessellation.

The determination of the local density around galaxies using either method strongly depends on several properties of the selected sample, such as its sensitivity in surface brightness and its completeness in total magnitude and redshift. Since these properties strongly depend on the adopted selection criteria used to define the sample, we decided to measure a density contrast for each galaxy. This is done as in Gavazzi et al. (2010). We first define the local density of the field:

$$\rho_{\rm field} = \frac{N_{\rm field}}{Area_{\rm field}}, \tag{3}$$

where $N_{\rm field}$ is the number of field galaxies in $Area_{\rm field}$, the field region defined in Table 3, with GALEX exposures in the NUV band >800 s. This limit in the integration time secures the completeness of the sample down to stellar masses of ≃10^8 $M_\odot$. The density contrast measured at the position of each single galaxy is then defined as:

$$\Delta\rho = \frac{\rho}{\rho_{\rm field}} - 1, \tag{4}$$

where ρ is the local density around each galaxy estimated with either the cylinder filter or the Voronoi tassellation. Because of this definition, the density contrast of galaxies in the outskirts of the cluster is $\Delta\rho \simeq 0$. As shown in Fig. 1, $\rho_{\rm field}$ is determined by mainly using galaxies located in the southern extension of the Virgo cluster. This is known to be an overdense region with respect to the typical field. The density contrast $\Delta\rho$ determined with Eq. (4) gives just a contrast of density within the observed region and certainly underestimates the real density contrast between the different structures of the cluster and the general field. This, however, is sufficient for the purpose of this work, since we are interested in quantifying relative differences in local density over the surveyed region rather than determining absolute values.

The comparison of the density contrast estimates determined using the cylinder and the Voronoi tessellation method gives very consistent results. The Voronoi technique produces a dynamical range of densities that is much larger than the use of cylinder with a fixed radius, because it is an adaptive method. In this way, the highest densities are computed on smaller scales than with the cylinders (even with a fixed radius of 0.2 Mpc), resulting in a much higher density contrast. Since we want to explore variations of different physical parameters as a function of the environment, we decided to use the Voronoi density contrast in the following analysis to have the largest possible range in the parameter space. We check, however, that the main conclusions of this work are robust with regard to the use of the two different density estimators. The Voronoi method also has the advantage that it does not depend on any assumption on the size of the adopted cylinder. We recall, however, that it might underestimate the local density of galaxies at the boundary regions of the Virgo cluster. Figure 4 shows the Voronoi tessellation of the Virgo cluster region done by using the whole sample of galaxies with redshift <3500 km s^{-1} and those done in different intervals of recessional velocity. All the different substructures previously identified are clearly visible in these figures. That is also the case for the LVC, which is clearly evident in the Voronoi tessellation plot done for galaxies with recessional velocity $vel < 400$ km s^{-1}.

7. The analysis

7.1. The 2D distribution of galaxies within the cluster

Besides helping us in the identification of the different cluster substructures, Fig. 1 clearly shows that galaxies belonging to the red sequence are preferentially located in the high density regions. The only exception are the M and LVC clouds, where red sequence, green valley, and blue cloud objects are well mixed. This evidence is a further confirmation of the well known morphology segregation effect (e.g. Dressler 1980; Whitmore et al. 1993) that is known to extend to the dwarf population in the Virgo cluster (Binggeli et al. 1988). Figure 1 also shows that the highest concentrations of quiescent systems roughly correspond to the peaks of the X-ray emission, where the density of the

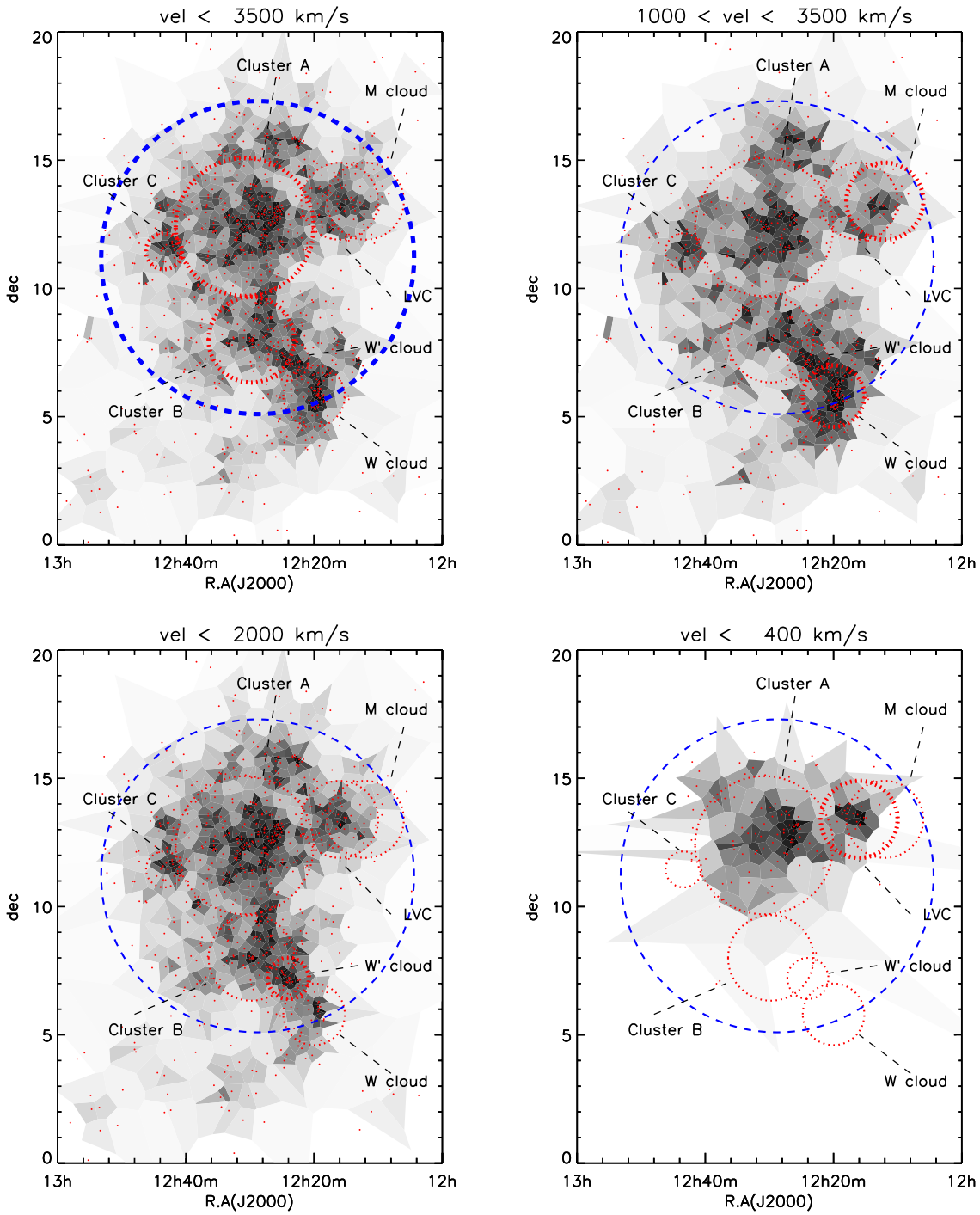

Fig. 4. Voronoi tessellation of the Virgo cluster region with darkness increasing according to the local density. The four plots show the Voronoi tessellation done by using the whole sample of galaxies with recessional velocity <3500 km s^{-1} (*upper left*), and in three subsamples in the velocity space: 1000 < *vel* < 3500 km s^{-1} (*upper right*), *vel* < 2000 km s^{-1} (*lower left*) and *vel* < 400 km s^{-1} (*lower right*). Red dots indicate the galaxies. The different cluster substructures and the region defining the field are identified with red-dotted and blue-dashed circles. Thicker contours are used whenever the structure has been identified within that velocity range with the only exception of the M cloud (see Table 3).

intracluster medium is at its maximum (Schindler et al. 1999)[6]. The X-ray map of Böhringer et al. (1994) does not extend below 6° in declination; we, thus, do not know whether the W cloud is also associated to a peak in the X-ray emission. In other words, the X-ray emission is a good tracer of the potential well of the different cluster substructures.

7.2. The colour-stellar mass relation within the substructures

Another way to study the dependence of the mean spectrophotometric properties of galaxies as a function of environment is to determine their $NUV - i$ vs. $M_{\rm star}$ relations separately for

[6] Schindler et al. (1999), however, noticed that while the X-ray emission of the cluster is peaked on M87, that of galaxies is ∼1 deg northwest of M87 in the direction of M86.

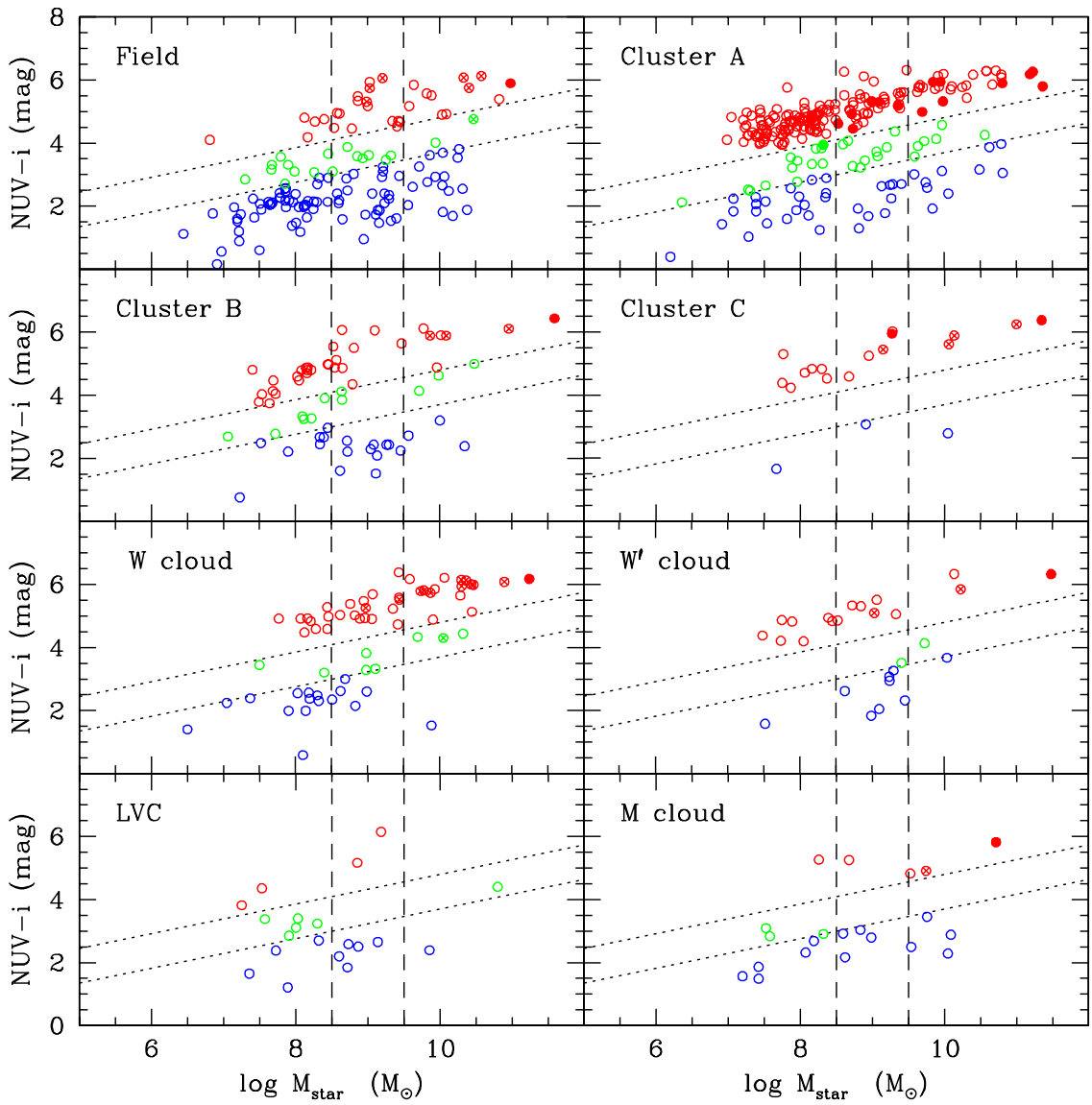

Fig. 5. Extinction corrected $NUV - i$ (AB system) vs. $M_{\rm star}$ relations for galaxies selected according to their substructure membership as defined in the text. Red, green, and blue colours are for galaxies in the red sequence, green valley, and blue cloud, respectively. Filled symbols are for slow rotators; crosses are for fast rotators. The vertical dashed lines show the interval in stellar mass used to define massive, intermediate, and low-mass objects within the sample.

the different cluster substructures (Fig. 5). Figure 5 confirms the claim of the previous section that all the identified regions with the exception of the M and LVC clouds are dominated by quiescent red galaxies, while galaxies at the periphery of the cluster (field) are mainly late-type systems. It also shows that the most massive galaxies ($M_{\rm star} \gtrsim 10^{11}\ M_\odot$), which are all red early-types with the exception of the spiral NGC 4216 in the LVC, are the dominant galaxies in all the substructures regardless their size or number of objects. Again, the M cloud could be considered as an exception because its most massive object, NGC 4168, has a stellar mass of only $M_{\rm star} = 10^{10.73}\ M_\odot$. Among the analysed substructures, we recall that the M cloud is the one with the lowest galaxy density (Table 3). On the contrary, galaxies with stellar masses $M_{\rm star} \gtrsim 10^{11}\ M_\odot$ are lacking in the field.

At the faint end of the colour-stellar mass relation for $M_{\rm star} \lesssim 10^{8}\ M_\odot$, Fig. 5 also shows a systematic difference in the galaxy population between the field and the densest regions, especially for Virgo cluster A. Indeed, in this stellar mass range, the core of the cluster is dominated by red quiescent dwarf ellipticals while these objects in the field are totally lacking. The other substructures with the exception of the M and LVC clouds seem to share the properties of cluster A (the observed small shift in the limiting stellar mass of the different subsamples is due to their higher distance, see Table 3). The observed difference with the field, on the other hand, can be partly due to a selection bias that favors the detection of blue objects in the periphery of the cluster where the survey is shallower than in the core (see Fig. 1).

We can also study the radial variation within the cluster of the mean spectrophotometric properties of galaxies by plotting the red-to-blue galaxy ratio as a function of the angular distance from the core of Virgo cluster A (θ) and the mean value for the other cluster substructures (cluster B and C, plus W, W′, M, and LVC clouds) and as a function of the density contrast ($\Delta\rho$) for galaxies in three different bins of stellar mass (Fig. 6). Figure 6 clearly shows that the radial variation of the red-to-blue galaxy ratio from the core of cluster A to ∼2 virial radii is small in massive systems (a factor of ∼3), while it is important in intermediate mass and in dwarf galaxies (≳20). This trend is even stronger

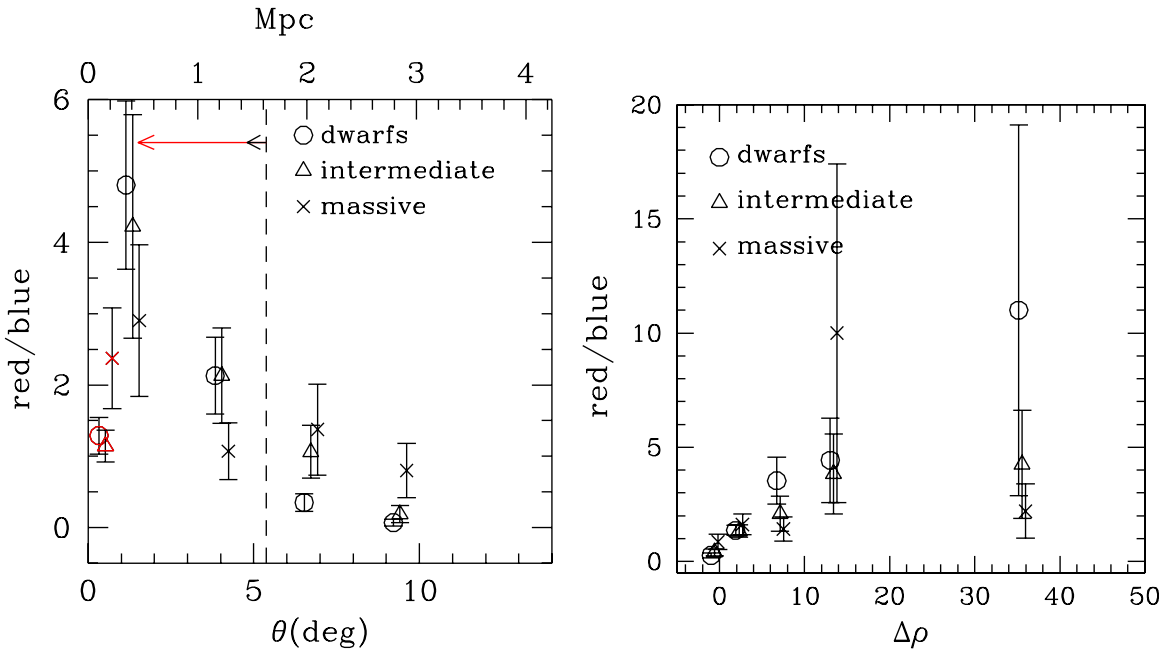

Fig. 6. *Left*: relationship between the red-to-blue galaxy fraction and the angular distance from the cluster centre for massive (crosses), intermediate (triangles) and low-mass (circles) galaxies belonging to cluster A or to the field (black symbols), as measured in bins of half virial radii (crosses and circles are slightly shifted along the X-axis to avoid confusion in the Poisson error estimate). Red symbols give the mean values for the other Virgo cluster substructures (clusters B, C and M, W, W′, and LVC clouds) at their mean angular distance determined in Mpc. The black dashed vertical line indicates the virial radius of cluster A. The black and red horizontal arrows show the mean distance covered by dwarf galaxies within the cluster during the time that they need to become HI-deficient (black) and red (red) after the quenching of their star-formation activity, as predicted by our models. *Right*: relationship between the red-to-blue galaxy fraction and the density contrast.

than the one observed by Haines et al. (2006a,b) in other nearby clusters. Only part of this trend can be due to selection biases (the outer regions are undersampled by GALEX at a sensitivity of the MIS). Indeed, these radial variations are already strong if they are limited to the intermediate stellar mass range, where the survey is expected to be fairly complete even at the periphery of the cluster. It is also clear if they are limited to the inner ∼1 virial radius with no restrictions on the stellar mass, where the survey is homogeneously complete at the depth of the MIS. A similar trend, although more scattered, is observed when the red-to-blue galaxy ratio is plotted vs. the density contrast. Curiously, the mean fraction of red-to-blue galaxies in the other cluster substructures is significantly lower than the one observed in the core of cluster A and does not significantly change with galaxy mass.

7.3. The colour-stellar mass relation as a function of the density contrast

An alternative way of testing the dependence of the colour-stellar mass relation on the environment is by plotting it in bins of $\Delta\rho$ as first proposed in the Coma supercluster by Gavazzi et al. (2010). This is done in Fig. 7, showing that the membership of galaxies to the red sequence, green valley, and blue cloud depends on the density in their surrounding. The red sequence is already formed in the lowest density regions in the outskirts of the cluster. Here, however, the fraction of red galaxies is significantly smaller than that of star-forming systems. We also notice that the number of massive red galaxies overcomes that of red dwarfs. We also observe that galaxies gradually populate the blue cloud, the green valley, and, finally, the red sequence with increasing density contrast. This effect is more pronounced in low-mass galaxies than in massive systems. In the highest density bins ($\Delta\rho > 10$), for instance, the galaxy population is dominated by red objects, consistently with Fig. 6. On the contrary, galaxies in the green valley are present mainly in the medium density bins ($0 < \Delta\rho < 10$).

7.4. The colour-stellar mass relation in the velocity space

A further step in the analysis of the spectrophotometric properties of galaxies within the cluster can be done by studying the distribution of red sequence, green valley, and blue cloud objects in the velocity space. To do that, we plot the relationship between $\frac{vel-\langle vel\rangle}{\sigma}$, where $\langle vel\rangle$ is the mean recessional velocity and σ is the velocity dispersion of cluster A, and the angular distance from the cluster core again for galaxies belonging to cluster A and to the field in Fig. 8. As defined, the parameter $\frac{vel-\langle vel\rangle}{\sigma}$ quantifies for each galaxy the excess of velocity along the line of sight with respect to the mean velocity dispersion of the cluster, providing useful information in the third dimension, while the angular distance from the cluster centre gives that on the plane of the sky. To combine these two different variables, we also plot the caustics determined in Fig. 8 as indicated in van Haarlem et al. (1993):

$$\frac{V_{\rm pec}}{H_0 r} \simeq -\frac{1}{3}\left[\frac{\langle\rho_{\rm cl}(r)\rangle}{\rho_{\rm c}}\right]^{0.75} \times \Omega_0^{-0.15}, \quad (5)$$

where $\rho_{\rm c} = \frac{3H_0^2}{8\pi G}$ is the critical density of the universe and $\rho_{\rm cl}(r)$ the mass density distribution within the cluster. The caustic is a useful tool to separate the infalling regions from the virialised part of the cluster. We calculate the radial density distribution $\rho_{\rm cl}(r)$ using the relation:

$$\rho_{\rm cl}(r) = \rho_0\left[1 + \frac{r^2}{r_{\rm c}^2}\right]^{-3\beta/2}, \quad (6)$$

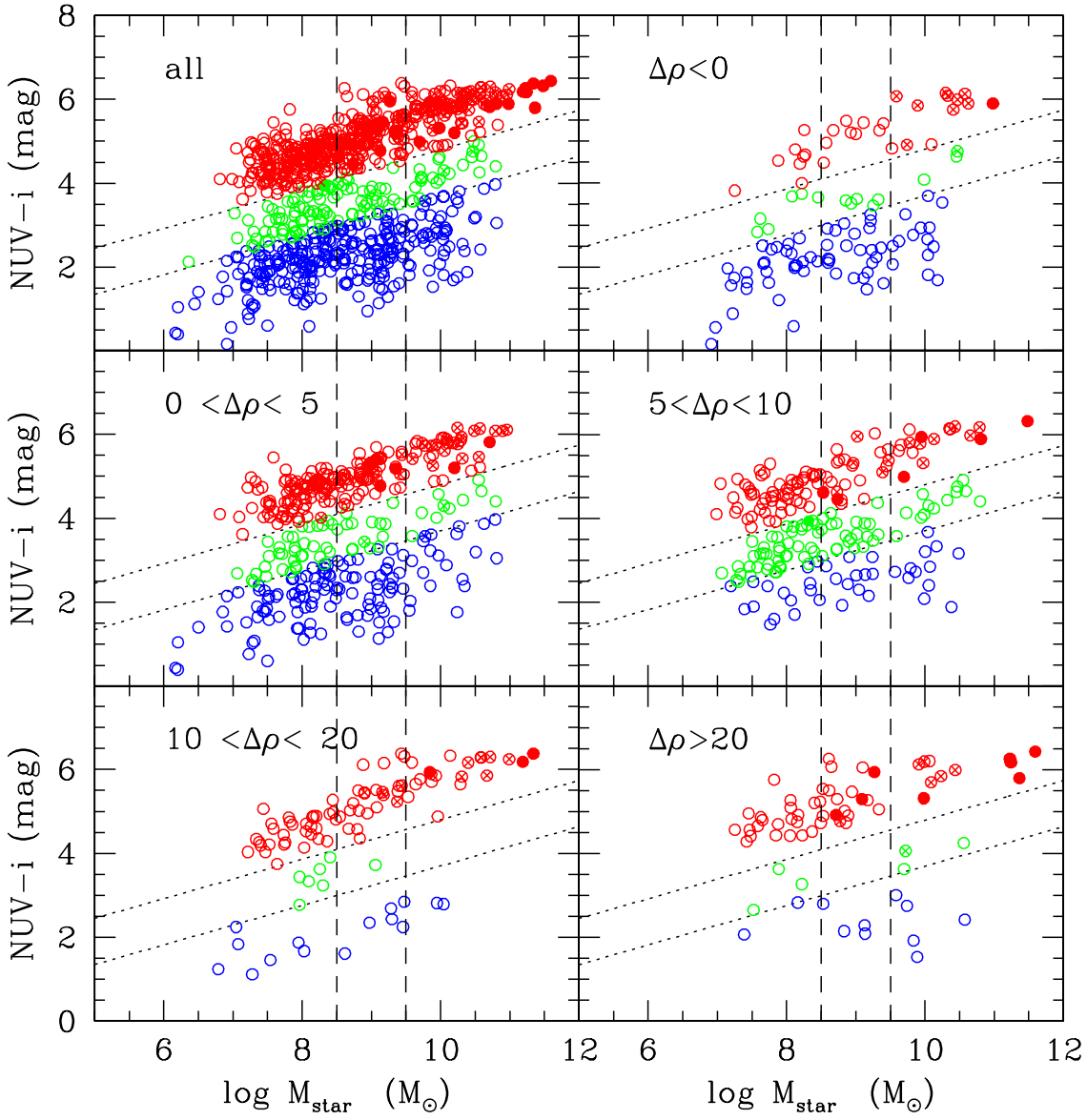

Fig. 7. Extinction corrected $NUV - i$ (AB system) vs. $M_{\rm star}$ relations for galaxies selected according to their density contrast. Red, green, and blue colours are for galaxies in the red sequence, green valley, and blue cloud, respectively. Filled symbols are for slow rotators; crosses for fast rotators. The vertical dashed lines show the interval in stellar mass used to define massive, intermediate, and low-mass objects within the sample.

assuming $r_{\rm c}$ = 65 arcmin and β = 0.75, as determined by Schindler et al. (1999) for the Virgo cluster. The variable ρ_0, for which we do not have any direct estimate, is chosen to ∼match the distribution of galaxies at low $\frac{vel-\langle vel\rangle}{\sigma}$ in Fig. 8. The analysis of Fig. 8 gives three major results:

1) The inner regions of Virgo cluster A are almost totally devoid of unperturbed galaxies with a normal star-formation activity (blue cloud) and quiescent late-type systems belonging to the green valley to a lower extent, and this is regardless of their stellar mass. Within the caustics, the main galaxy population is that of red quiescent objects.
2) Within the central half virial radius (∼0.8 Mpc), the galaxies with the highest peculiar velocities with respect to the mean velocity of the cluster are red, quiescent dwarf systems. These are, thus, early-type dwarfs which recently entered the cluster.
3) The majority of the massive and intermediate slow rotators are located in the inner half virial radius and within the caustics, indicating that they are cluster members since the early formation of Virgo.

8. Discussion: A unified picture of galaxy evolution

In this section, we combine these new observational results to the prediction of our multizone chemo-spectrophotometric models of galaxy evolution with the purpose of understanding the role of the cluster environment in the formation of the red sequence. The analysis presented so far suggests that massive and dwarf galaxies behave in different ways. We thus address this discussion separately for massive and dwarf systems.

8.1. Massive galaxies

The star-formation activity of galaxies is tightly related to their content of atomic and molecular gas, as indicated by the Schmidt law (Schmidt 1959; Kennicutt 1998b; Bigiel et al. 2008). The

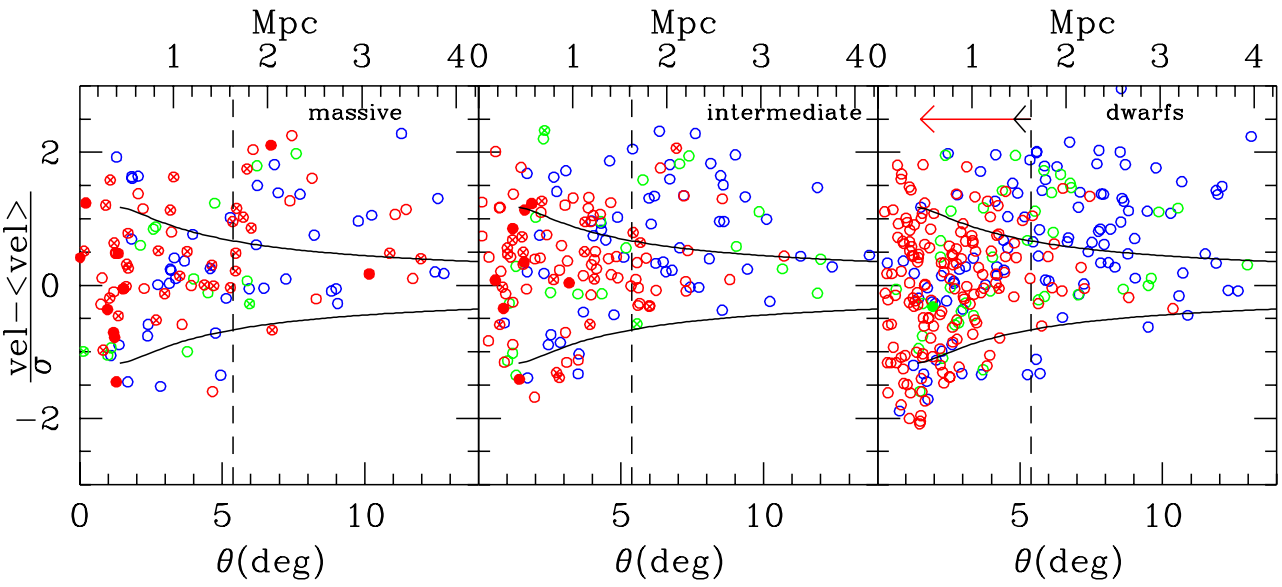

Fig. 8. Relationship between $\frac{vel-\langle vel\rangle}{\sigma}$ and the angular distance from the cluster centre for massive, intermediate and low-mass galaxies in cluster A and in the field. Red, green, and blue colours are for galaxies in the red sequence, green valley, and blue cloud, respectively. Filled symbols are for slow rotators, crosses for fast rotators. The black dashed vertical line indicates the virial radius of the cluster. The solid lines indicate the caustics that are drown to identify the gravitationally bounded region of cluster A. The black and red horizontal arrows show the mean distance covered by dwarf galaxies within the cluster during the time that they need to become HI-deficient (black) and red (red) after the quenching of their star-formation activity, as predicted by our models.

gaseous component, especially the atomic phase, which is located on an extended disc in spiral galaxies, can be easily removed during any kind of interaction with the hostile cluster environment (e.g. Boselli & Gavazzi 2006). Figure 9 shows the distribution of HI-normal ($HI-def \leq 0.4$) and HI-deficient ($HI-def > 0.4$) late-type galaxies within the Virgo cluster region. Figure 9 indicates that gas-rich, massive galaxies are not present in the high-density regions associated to the X-ray emitting gas in cluster A (e.g. Cayatte et al. 1990). This observational result has been historically interpreted as strong evidence of ram pressure stripping. The same galaxies are also rare in the other high-density substructures with the exception of the M cloud, as firstly noticed by Gavazzi et al. (1999), and in the LVC. The lack of gas in both its atomic (Hughes & Cortese 2009; Cortese & Hughes 2009; Gavazzi et al. 2013a,b) and molecular (Fumagalli et al. 2009; Boselli et al. 2014) phase quenches the activity of star formation, making HI-deficient cluster galaxies redder than unperturbed objects. To see the effects of gas stripping on the stellar population of galaxies, we plot in Fig. 10 the $NUV-i$ vs. $M_{\rm star}$ relation for all galaxies of the sample and compare this diagram to the predictions of the models. Figure 10 shows that the ram pressure gas stripping due to a single crossing of the cluster is not sufficient to fully stop the activity of star formation of infalling massive late-type galaxies. Gas deficient late-type galaxies with a residual activity of star formation that make them fall in the green valley are indeed still present on the innermost regions of the cluster. The $NUV-i$ colour of these gas stripped galaxies does not become as red as the one of similar stellar mass objects on the red sequence (Cortese & Hughes 2009). As extensively discussed in Boselli et al. (2014), the total gas removal via ram pressure stripping requires timescales on the order of 1.5 Gyr in these massive objects, as indicated by recent hydrodynamic simulations (Tonnesen & Brayan 2009; Roediger & Bruggen 2007). These timescales have been determined using tuned simulations that are able to reproduce the different gas phases from the densest molecular gas located inside

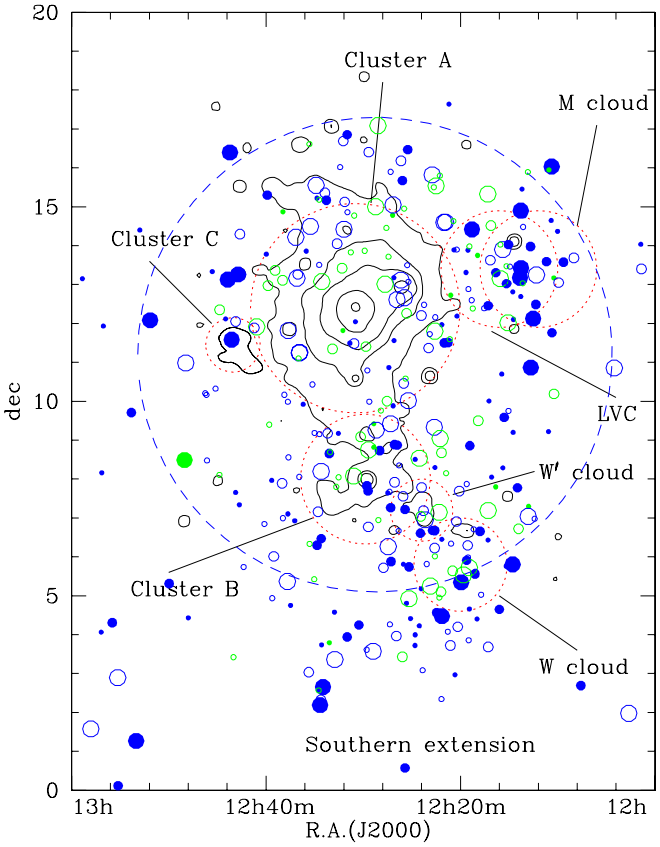

Fig. 9. Sky distribution of star-forming galaxies with colours of the symbols coded in Fig. 2. Filled symbols indicate galaxies with a normal HI content ($HI-def \leq 0.4$), empty symbols HI-deficient galaxies ($HI-def > 0.4$). The size of the symbols is proportional to the stellar mass of galaxies: big symbols are for galaxies with $M_{\rm star} > 10^{9.5}\ M_{\odot}$; medium size symbols for objects with $10^{8.5} < M_{\rm star} \leq 10^{9.5}\ M_{\odot}$; small size symbols for $M_{\rm star} \leq 10^{8.5}\ M_{\odot}$.

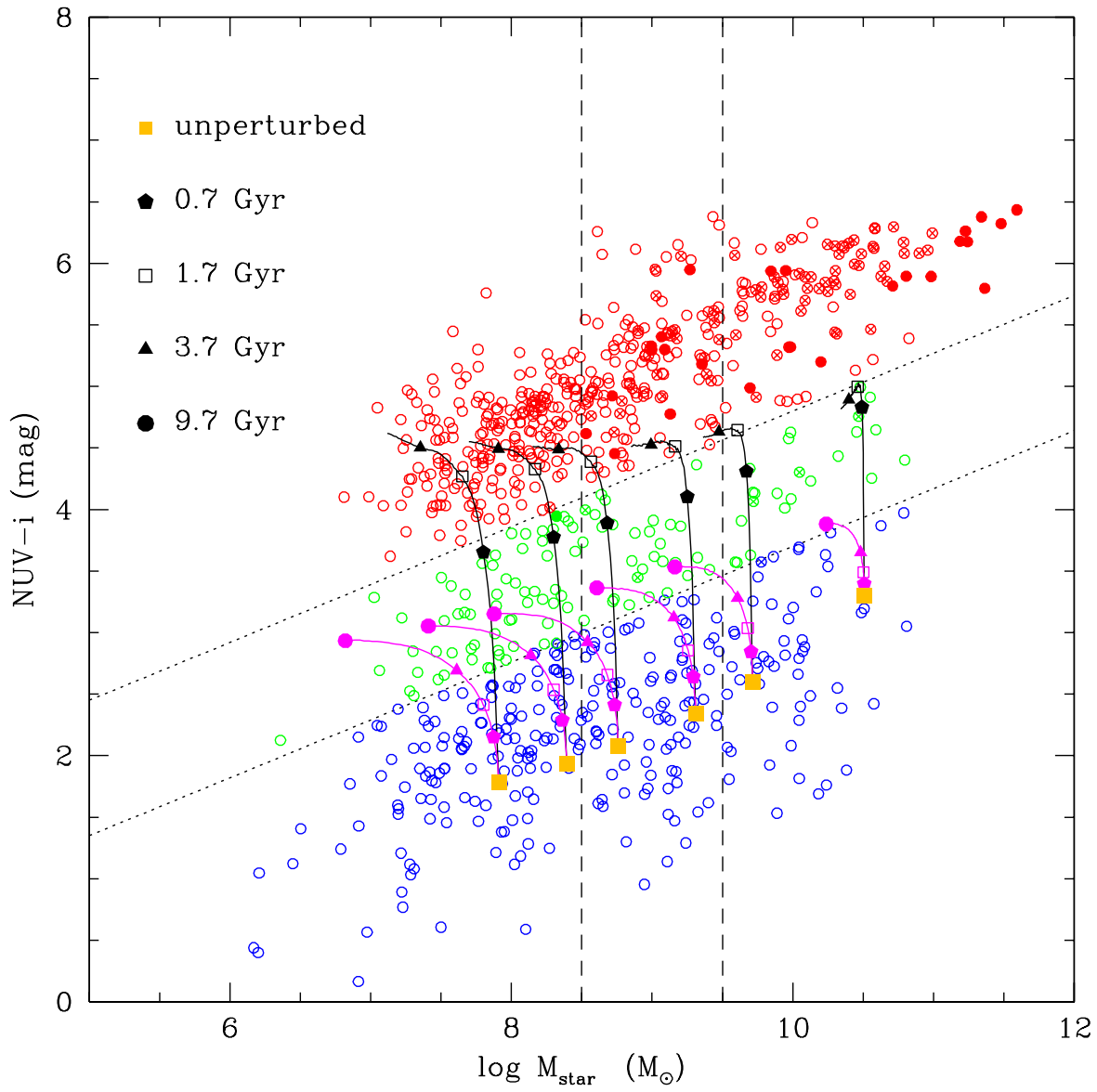

Fig. 10. Extinction corrected $NUV - i$ (AB system) vs. $M_{\rm star}$ relation for all galaxies of the sample. Filled symbols are for slow rotators; crosses are for fast rotators. Symbols are colour coded as in Fig. 2. The large orange filled squares indicate the models of unperturbed galaxies of spin parameter $\lambda = 0.05$ and rotational velocity 40, 55, 70, 100, 130, 170, and 220 km s^{-1}. The magenta lines indicate the starvation models. The black lines show the ram pressure stripping models. Different symbols along the models indicate the position of the model galaxies at a given look-back time from the beginning of the interaction.

giant molecular clouds to the diffuse gas of the ISM (Tonnesen & Bryan 2009). They also consider the change in the impact parameter that a galaxy encounters along its orbit within the cluster (Roediger & Bruggen 2007). These timescales are relatively short because these recent models are also able to strip the molecular gas phase, as now confirmed by observations (Fumagalli et al. 2009; Boselli et al. 2014). Once the gas is removed, the delay in the quenching of the star-formation activity is ∼0.8 Gyr longer, thus on the order of ∼2.3 Gyr. This timescale is longer than the typical crossing time of the cluster (∼1.7 Gyr; Boselli & Gavazzi 2006). It is thus not surprising that gas-poor, freshly infalling star-forming massive galaxies are located all over the cluster, since they do not have the time to totally stop their activity and become red objects before reaching the cluster core. This process of migration from the blue cloud to the red sequence is now also reproduced in cosmological simulations (e.g. Cen 2014).

Figure 10 also shows that galaxy starvation is not able to create the red sequence just by quenching the star-formation activity through gas consumption once the infall of pristine gas is stopped. The models shown in Fig. 10 produce late-type galaxies that are too blue compared to red sequence objects even if the starvation process started ∼10 Gyr ago (oldest plotted model). Using the same models, Cortese et al. (2011) have shown that starvation cannot reproduce the observed HI scaling relations of gas-poor cluster galaxies. This result is fully consistent with what is presented in Boselli et al. (2006) for NGC 4569. The starvation process is not able to produce the truncated radial profiles typical of gas stripped galaxies. This process is also expected to significantly decrease the mean effective surface brightness of the perturbed galaxies. Starvation is thus inconsistent with observations, since it is known that the mean effective surface brightness of lenticular galaxies, which are the potential output of the starvation process, is brighter than that of star-forming

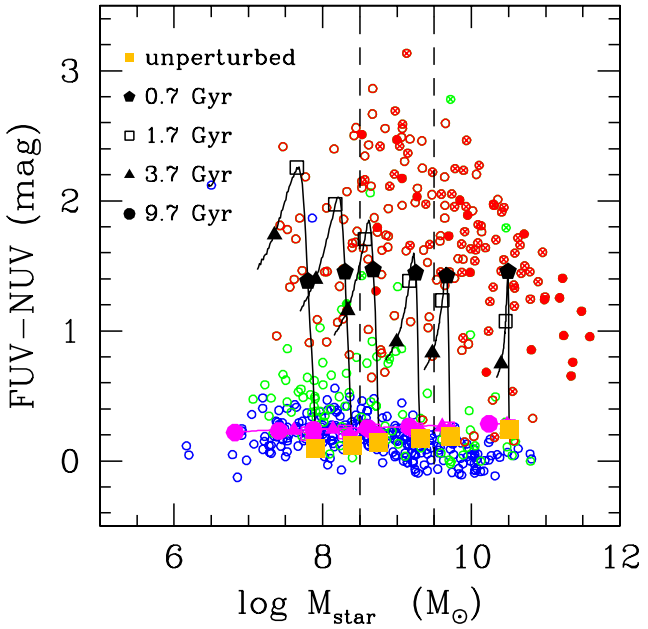

Fig. 11. Extinction corrected $FUV - NUV$ (AB system) vs. $M_{\rm star}$ relation. Symbols, dotted, and dashed lines and models are as in Fig. 10.

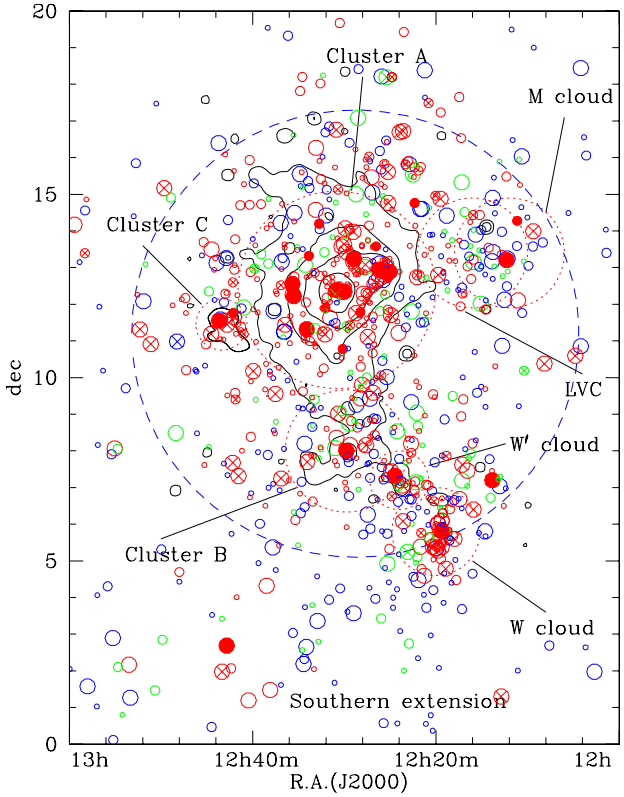

Fig. 12. Sky distribution of galaxies with colours of the symbols coded as in Fig.2. Filled symbols indicate slow rotators; crosses are fast rotators. The size of the symbols is proportional to the stellar mass of galaxies: big symbols are for galaxies with $M_{\rm star} > 10^{9.5}\ M_\odot$, medium size symbols for objects with $10^{8.5} < M_{\rm star} \leq 10^{9.5}\ M_\odot$, and small size symbols for $M_{\rm star} \leq 10^{8.5}\ M_\odot$.

systems of similar mass (Boselli & Gavazzi 2006). In galaxies recently stripped of their gas, the timescale for gas consumption, which is determined considering the atomic and molecular gas phase plus the recycled phase produced by stars during their evolution ($\tau_{{\rm gas},R} \simeq 3.0$–$3.3$ Gyr), is also significantly longer than the timescale for complete gas stripping via ram pressure, making starvation an improbable mechanism for quenching the activity of star formation in massive galaxies in clusters (Boselli et al. 2014). We recall, however, that the original definition of starvation proposed by Larson et al. (1980) considers that the consumption of gas via star formation happens once the halo of the hot gas surrounding galaxies, which is expected to feed the stellar disc, is removed during the interaction. This definition is slightly different than the one adopted in our models, which is based on the assumption that gas infall is stopped. Our models, however, do not consider a hot halo of gas but only the gaseous component located on the disc thus they should be representative of the general definition often used in cosmological and semianalytic models.

Figure 10 also reveals that the most massive red galaxies with $M_{\rm star} \gtrsim 10^{10.7}\ M_\odot$ do not have similar counterparts in the blue cloud nor in the green valley. It is thus impossible that a simple quenching of the star-formation activity of a late-type galaxy forms these massive, red systems. The quenching of the star-formation activity, indeed, prevents the secular increase of the stellar mass that is typical of unperturbed objects and produces perturbed galaxies of lower stellar mass then their isolated counterparts. The most massive red galaxies have stellar masses as high as $M_{\rm star} \simeq 10^{11.5}\ M_\odot$ thus, the observed shift in the bright end between the red sequence and blue cloud galaxies cannot be due to a systematic error in the stellar mass determination of the two different populations (see Appendix B). Figure 10 shows that the majority of these massive ($M_{\rm star} \gtrsim 10^{10.7}$) red, early-type galaxies are slow rotators. Following the arguments of Cappellari et al. (2011b) and Cappellari (2013), it is thus conceivable that these objects have been formed through major merging events. This is a violent process that can dynamically heat the system and transform on short timescales the full amount of gas into stars and producing pressure supported, gas poor roundish objects characterised by old stellar populations (e.g. Barnes 1992; Barnes & Hernquist 1996). The $FUV - NUV$ vs. $M_{\rm star}$ relation plotted in Fig. 11, which is sensitive to the presence of young populations in star-forming systems and to very old stars in evolved objects (the UV upturn, O'Connell 1999; Boselli et al. 2005) suggests that these most massive galaxies are also those with the oldest stellar populations (Bureau et al. 2011). This evidence suggests that the major merging events happened at very early epochs. This picture is consistent with what is shown in Fig. 8, where all but one of the slow rotators of cluster A are located within the caustic, indicating their membership to the virialised component of the cluster. They are thus within the densest regions since an early age.

Figure 12 shows the distribution of galaxies within the Virgo cluster region using different symbols to identify fast and slow rotators. Combined with Fig. 5, Fig. 12 shows that these slow-rotating massive early-type galaxies are the most massive objects of each single substructure within the cluster. Indeed this is the case for M87 in cluster A, M49 in cluster B, NGC 4168 in the M cloud, NGC 4261 in the W cloud, and NGC 4365 in the W′ cloud. The most massive galaxy of Virgo cluster C, M60 (NGC 4649), is classified in Emsellem et al. (2011) as a fast rotator. We notice, however, that if we calculate the limiting spin parameter $\lambda_{\rm Re}({\rm lim})$ below which that galaxy is considered as a slow rotator, $\lambda_{\rm Re}({\rm lim}) = 0.31\sqrt{\epsilon}$, where ϵ is the ellipticity of the galaxy, by using the photometric dataset of Cortese et al. (2012a) for the *Herschel* Reference Survey in the i-band ($\epsilon = 0.19$), $\lambda_{\rm Re}({\rm lim}) = 0.135$, while the observed value is $\lambda_{\rm Re} = 0.127$.

The object M60 could thus be considered as a slow rotator as all the other most massive galaxies of each single cluster substructure. The only exception is NGC 4216 in the LVC, which is a massive, HI-deficient spiral galaxy classified as SAB(s)b: in NED. We can thus conclude that all the most massive galaxies ($M_{\rm star} \gtrsim 10^{11}\ M_\odot$) in groups characterised by velocity dispersions of $200 \lesssim \sigma \lesssim 550$ km s^{-1} have been formed by major mergers. Among these groups, those included in the ROSAT image of Böhringer et al. (1994) are also charaterised by a diffuse X-ray emission. Being the X-ray gas a direct tracer of the potential well, this is the first direct evidence that the dominant galaxies of massive haloes are slow rotators, as expected but never observed so far (Scott et al. 2014). This picture is consistent with the semianalytic models of De Lucia et al. (2006), which indicate that only the most massive early-type galaxies ($M_{\rm star} \gtrsim 10^{11}\ M_\odot$) are formed by major merging events. It is also consistent with the semianalytic predictions of Khochfar et al. (2011), which indicate that slow rotators are preferentially central galaxies associated with a large halo. It also matches with the observational work of Wilman & Erwin (2012), who concluded using different arguments that central galaxies of massive haloes are ellipticals formed by major merging events. On a more general context, they also confirm that slow rotators are primarily situated in high-density regions (Cappellari et al. 2011; Cappellari 2013; Houghton et al. 2013; D'Eugenio et al. 2013; Scott et al. 2014).

In the Virgo cluster A, however, there are quite a few galaxies with stellar masses down to $\sim 10^{10}\ M_\odot$ (corresponding to the limiting stellar mass of the ATLAS^{3D} survey) that are slow rotators, and at the same time, there are a few fast rotators with $M_{\rm star}$ as high as $\sim 10^{11}\ M_\odot$. Slow rotators are mainly located inside the inner half virial radius (Fig. 12) and are preferentially virialised within the cluster potential (Fig. 8). It is thus conceivable that they have been formed by a merging event early in the past, when galaxies and groups were smaller than at the present epoch. The most massive fast rotators have stellar masses that are not significantly larger than those of star-forming discs, and thus we cannot exclude that they have been formed through less violent phenomena. The considerations given above on the higher effective surface brightness of massive lenticulars with respect to that of similar late-type systems suggest that gravitational interactions, which are efficient at early epochs when galaxies were accreted in infalling groups (pre-processing), rather than a simple ram pressure stripping event, is at the origin of this population (e.g. Boselli & Gavazzi 2006; Dressler 2004; Wilman et al. 2009; Boundy et al. 2010; Dressler et al. 2013). Multiple gravitational interactions (galaxy harassment, Moore et al. 1998) are indeed able to induce the formation of bars with nuclear gas infall, thus producing thicker discs than those formed through a mild, secular evolution. Clearly, a full understanding of the kinematical properties of the Virgo cluster galaxies would benefit from a larger dataset also including late-type systems.

8.2. Dwarf galaxies

This new set of observations and the models are fully consistent with the evolutionary picture originally presented in Boselli et al. (2008a,b) for dwarf systems. Boselli et al. (2008a) and Gavazzi et al. (2013a) estimated a high infall rate of dwarf galaxies in the Virgo cluster (~300 galaxies Gyr^{-1}). The ram pressure stripping exerted by the hot and dense intergalactic medium on these dwarf galaxies moving at high velocity within the cluster is sufficient to fully remove their total gaseous component on very short timescales ($\lesssim$200 Myr), as indeed shown in Fig. 9. Because of the lack of gas, the infalling galaxies stop their activity of star formation, and become red systems in $\simeq$1 Gyr. Figure 10 clearly shows that this process is so efficient to transform star-forming galaxies in quiescent systems as red as those populating the red sequence. The efficiency even increases with multiple crossings of the cluster (Boselli et al. 2008a). The analysis presented so far, made possible thanks to the full coverage of the Virgo cluster region at different frequencies, confirms this scenario. The most recent hydrodynamical simulations (Roediger & Bruggen 2007; Tonnesen & Bryan 2009; Cen et al. 2014) and the observation of star-forming galaxies with HI (e.g. Scott et al. 2012), Hα (e.g. Yagi et al. 2008), and X-ray (Sun et al. 2010) tails of stripped material at the periphery of clusters consistently indicate that ram pressure stripping is efficient even outside the virial radius of massive clusters, such as Virgo. Given that this process is able to transform star-forming systems into red objects on timescales of $\simeq$1 Gyr, and that these freshly infalling objects are moving on the plane of the sky with a velocity with respect to the cluster centre of $\sigma = 1150$ km s^{-1} (the typical velocity dispersion of late-type galaxies in the cluster, from Boselli & Gavazzi 2006), we expect that most of them are fully transformed before they reach the cluster core. This would thus explain the observed variation of the red-to-blue fraction with the angular distance from the cluster centre or the trend with local density observed in Figs. 6 and 7. This picture is also consistent with what observed in Fig. 8. The presence of red dwarf galaxies within the inner region of cluster A but outside the caustic, thus not belonging to the virialised component, suggests that the infall of these systems is relatively recent.

The unique coverage at different wavelengths of the whole Virgo cluster region can be used to test whether this scenario is consistent also with other observations. To do that, we plot the distribution of dwarf and intermediate stellar mass galaxies ($M_{\rm star} \leq 10^{9.5}\ M_\odot$) within the Virgo cluster region using different symbols to indicate whether they contain some cold dust in their interstellar medium, whether they have a residual nuclear star-formation activity or whether they are in a post-starburst phase (see Sect. 3) in Fig. 13. Dusty galaxies are identified using the 250 μm SPIRE band emission (detected galaxies), where the sensitivity of *Herschel* is at its maximum[7]. We also plot in Fig. 14 the distribution of the colour difference $(NUV - i) - (NUV - i)_{\rm Mod}$, where $(NUV - i)_{\rm Mod}$ is the colour of the unperturbed model galaxy (see Sect. 5) for the galaxies observed by *Herschel* (upper panels), with nuclear star-formation activity (central panels), and for post-starbursts (PSB; lower panels), where galaxies are separated in three bins of stellar mass. We recall that this plot shows the mean displacement in $NUV - i$ colour from the typical blue cloud colour-stellar mass relation. Given the homogeneous depth of the HeViCS survey, the *Herschel* data can be used to identify dust-rich galaxies over the mapped region, which unfortunately covers only a fraction of the GUViCS fields (see Fig. 1). Figure 13 shows that dusty galaxies, especially those of low stellar mass, tend to avoid the X-ray emitting regions within cluster A and B. We notice, however, several dust-rich dwarf red galaxies in those cluster substructures not characterised by a diffuse X-ray emission (W, M, and LV clouds). Figure 14 indicates the presence of dust in spiral galaxies in the blue cloud and in the green valley down to $\sim 10^8\ M_\odot$, while most of the detected red galaxies have stellar masses larger than $\sim 10^{9.5}\ M_\odot$ (De Looze et al. 2013). The fraction of dusty galaxies with red colours, however,

[7] For this particular band, we limit the analysis to those dwarf galaxies that are potentially detectable by *Herschel* ($10^8 \leq M_{\rm star} \leq 10^{9.5}\ M_\odot$).

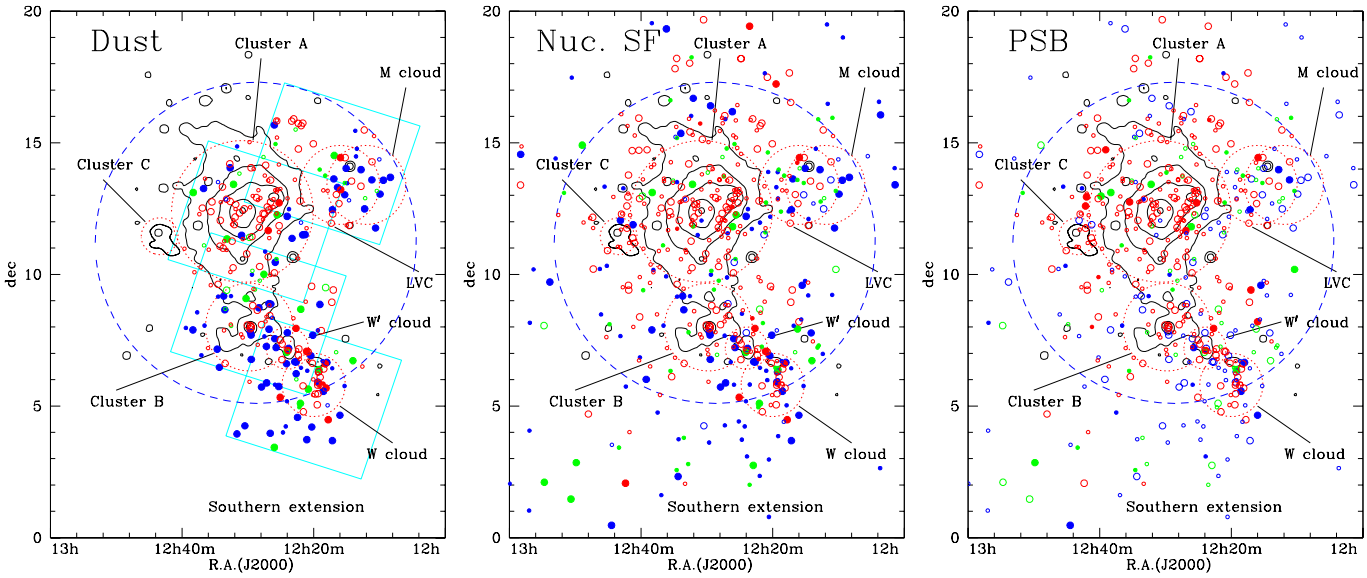

Fig. 13. *Left*: sky distribution of the subsample of galaxies observed by *Herschel*. Red, green, and blue symbols are used to indicate galaxies belonging to the red sequence, green valley, and blue cloud, respectively. Filled dots indicate dust-rich galaxies, while empty symbols are undetected objects. The size of the symbols is proportional to the stellar mass of galaxies: medium size symbols are for objects with $10^{8.5} < M_{\rm star} \leq 10^{9.5}\ M_{\odot}$, small size symbols for $10^{8} \leq M_{\rm star} \leq 10^{8.5}\ M_{\odot}$. *Centre*: sky distribution of the subsample of galaxies observed in spectroscopic mode by the SDSS. Filled dots indicate galaxies with an equivalent width in the Hα emission line $EW\,{\rm H}\alpha_{\rm emi} > 3$ Å (and $S/N > 5$), witnessing a nuclear star-forming activity. *Right*: same as central plot but where filled dots indicate PSB galaxies. In these last two plots, medium size symbols are for objects with $10^{8.5} < M_{\rm star} \leq 10^{9.5}\ M_{\odot}$; small size symbols are for $M_{\rm star} \leq 10^{8.5}\ M_{\odot}$.

continuously decreases with decreasing stellar mass. In the intermediate stellar mass range ($10^{8.5} \lesssim M_{\rm star} \lesssim 10^{9.5}\ M_{\odot}$), the few objects detected at 250 μm belonging to the red sequence are those with the bluest colours. In the lower stellar mass range ($M_{\rm star} \lesssim 10^{8.5}\ M_{\odot}$) none of the red sequence objects have been detected by *Herschel*, while only half of those belonging to the green valley and the majority in the blue sequence.

Figure 13 shows also the presence of several red galaxies with a residual nuclear star-formation activity or in a post-starburst phase. They are mainly located in the cluster periphery or in those substructures that are not characterised by a diffuse X-ray emission (W, M, and LV clouds). They often correspond to the dust-rich red galaxies detected by *Herschel*. Within cluster A (at a radial distance smaller than half the virial radius, roughly corresponding to the X-ray emitting region), the number of dwarf galaxies of stellar mass $10^{8} < M_{\rm star} < 10^{9.5}\ M_{\odot}$ observed by *Herschel* down to its detection limit with spectroscopic data is 78. Out of these, only 11 are dust-rich objects (14%). Among those with a nuclear star-formation activity, the fraction of dusty objects increases up to 58% (7/12), while dwarf far-infrared detected objects are 62% (5/8) among PSB galaxies. Similar ratios are obtained when the analysed region is extended to the whole *Herschel* field, thus adding the other main substructures of the cluster (Fig. 13). Figure 14 shows that PSB galaxies, which are those objects that recently abruptly stopped their nuclear star-formation activity, are galaxies of intermediate or low stellar mass. Although present in the blue cloud, PSB galaxies are preferentially located in the green valley or among the bluest objects in the red sequence (Gavazzi et al. 2010). They are frequent only at low and intermediate stellar masses. Galaxies with a nuclear star-formation activity are preferentially late-type systems both belonging to the blue cloud and to the green valley. This indicates that the quenching of the star-formation activity is principally in the outer disc of spirals. There are, however, a few dwarf early-type galaxies in the red sequence of intermediate or low stellar mass where star formation is still present in their nucleus.

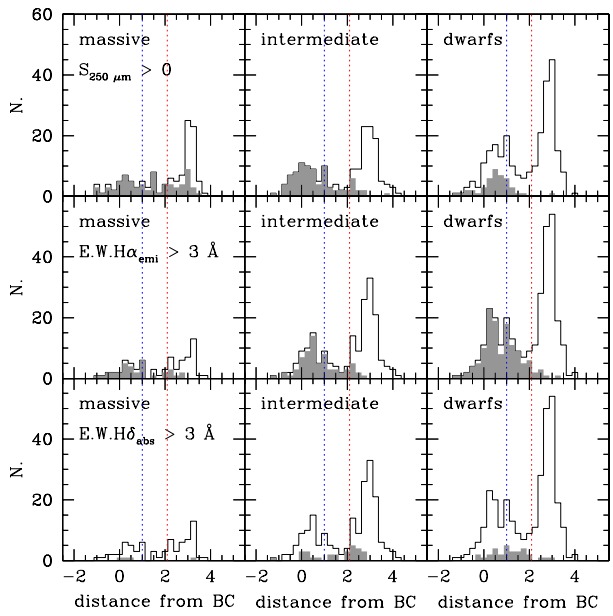

Fig. 14. Distribution of the colour difference $(NUV - i) - (NUV - i)_{\rm Mod}$ corresponding to the mean distance from typical colour-stellar mass relation of blue cloud (BC) objects for massive ($M_{\rm star} > 10^{9.5}\ M_{\odot}$; *left*), intermediate ($10^{8.5} < M_{\rm star} \leq 10^{9.5}\ M_{\odot}$; *centre*), and dwarf ($M_{\rm star} \leq 10^{8.5}\ M_{\odot}$; *right*) galaxies. The *upper row* shows the distribution of galaxies observed (black histogram) and detected (grey shaded histogram) by *Herschel*; the *middle and lower rows* are the distributions of objects with available nuclear spectroscopy from SDSS (black) with a nuclear star-formation activity (grey) or in a post-starburst phase (grey), respectively. The vertical red and blue dotted lines indicate the limits used to identify the red sequence and the blue cloud.

To summarise, the observations collected so far combined with hydrodynamical simulations and our specrophotemetric models of galaxy evoultion consistently indicate that the ram

pressure exerted on the dwarf galaxy population that infalls into the cluster is able to remove the atomic gas on short timescales. The stripping process starts to be efficient outside the virial radius, as indicated by the presence of HI-deficient galaxies up to ∼2 virial radii (Gavazzi et al. 2013a and Fig. 9). In a ram pressure stripping process, both gas and dust are stripped outside-in (e.g. Boselli et al. 2006; Fumagalli & Gavazzi 2008; Cortese et al. 2010, 2012b). Some gas and dust can be retained in the nuclear regions, where the potential well is at its maximum, as indicated by high resolution *Herschel* images (de Looze et al. 2010, 2013). This happens mainly in the most massive dwarfs or in those objects located outside the X-ray emitting regions, where gas stripping is expected to be less efficient. Gas removal quenches the activity of star formation, making galaxies redder. The activity of star formation, however, can last longer in the nuclear regions where some gas and associated dust can be still retained.

This scenario is also confirmed by the recent kinematic observations of Toloba et al. (2009, 2011, 2012, 2014). Indeed, a large fraction of dwarf elliptical galaxies with stellar masses $10^{8.5} < M_{\rm star} < 10^{9.5}\ M_\odot$ within Virgo are rotationally supported systems with rotation curves similar to those of late-type systems of comparable stellar mass. In a soft, ram pressure stripping event, the angular momentum must be conserved, without other violent gravitational interactions with nearby companions, the perturbed galaxies should conserve their rotation curve. In this picture, fast rotators have been formed after a mild ram pressure stripping event able to remove the whole gas content of a low-mass rotating disc, while slow rotators are the result of more violent gravitational interactions. As first noticed by Toloba et al. (2009), fast rotators are preferentially situated at the periphery of the cluster. Contrary, slow rotators are preferentially located close to the highest density regions within the X-ray emitting gas in cluster A (eight out of the ten slow rotators of the sample; see Fig. 12). They are also mainly situated within half the virial radius and within the caustics (7/10), suggesting that they belong to the virialised population inhabiting the cluster since its formation (Conselice et al. 2001). It is thus conceivable that the harassment induced by multiple encounters with other members and with the potential of the cluster as a whole, which is efficient on relatively long timescales, had the time to perturb these galaxies, producing roundish, high surface brightness, pressure supported objects (Benson et al. 2014; Toloba et al. 2014). Harassment, however, can hardly explain the formation of the whole dE galaxy population of Virgo. Indeed, the structural properties of harassed galaxies, as predicted by the models of Mastropietro et al. (2005), do not match the observed properties of typical dE in Virgo; instead they are well reproduced in a ram pressure stripping scenario (Boselli et al. 2008b). Furthermore, the long timescales required to perturb galaxies with multiple flyby encounters does not match with a recent formation of the faint end of the red sequence, as determined from the observations of high- and intermediate-redshift clusters (Kodama et al. 2004; De Lucia et al. 2004, 2007, 2009; Stott et al. 2007, 2009; Gilbank & Balogh 2008; Jaffe et al. 2011). It also does not mach with the large infall rate of star-forming low-mass systems inferred by Boselli et al. (2008a) and Gavazzi et al. (2013a). There is also additional evidence against preprocessing through galaxy harassment in dwarf galaxies within the groups infalling onto Virgo. Indeed, in these groups the red-to-blue galaxy ratio is significantly smaller than the one observed in the core of Virgo A, where most of the dE are located (see Fig. 6), suggesting that harassment is not particularly efficient in stopping the activity of star formation within the infalling groups. This is probably related to the reason that both the density and the velocity dispersion are significantly smaller than in massive clusters within these groups, thus keeping the process efficient only on long timescales. On the other hand, fast rotators are preferentially located outside half the virial radius and the caustic (13/21), suggesting that they are rotating systems that have recently fallen into the cluster. All their structural, spectrophotometric, and kinematic properties can be easily explained by a mild but rapid transformation after a ram pressure stripping event.

9. Conclusion

We study the origin of the red sequence in high-density environments using a multifrequency analysis of a large sample of galaxies located in the Virgo cluster and in its surroundings. The sample, which includes 868 galaxies extracted from the GUViCS survey (Boselli et al. 2011), is composed of galaxies spanning a wide range in stellar mass ($10^7 \lesssim M_{\rm star} \lesssim 10^{11.5}\ M_\odot$) and morphological type (from dwarf irregulars to massive ellipticals). We first identify the different substructures composing the cluster: Virgo cluster A, B and C, the W, W′, M and the LVC. We identify galaxies belonging to the red sequence, the green valley, and the blue cloud using their dust attenuation corrected $NUV - i$ colour index. We then study how galaxies belonging to these three different populations are located within the various cluster substructures. We observe a clear colour-segregation effect with red galaxies located principally in the highest density regions (cluster A, B, C, W, and W′), while blue star-forming systems mainly in the periphery of the cluster.

The most massive galaxies of the sample ($M_{\rm star} \gtrsim 10^{11}\ M_\odot$) are all early-type galaxies dominating the different substructures of the cluster with the exception of the M and LVC clouds. The majority of these substructures are also characterised by a diffuse emission of the intracluster gas, indicating that the associated massive ellipticals are also the dominant galaxies within the group dark matter halo. These galaxies are all pressure supported systems (slow rotators) probably formed by a major merging event occurred at early epochs, as suggested by their very old stellar populations at the origin of their pronounced UV-upturn. The other slow rotators of the sample are galaxies of intermediate-to-high stellar mass ($10^{8.5} \lesssim M_{\rm star} \lesssim 10^{11}\ M_\odot$) that are generally located within the core of the different cluster substructures and mainly in cluster A. Their recessional velocity distribution and position indicate that they are virialised systems within the cluster potential well and are thus cluster members since early epochs.

All galaxies located within the inner regions of cluster A, where the density of the intracluster medium is at its maximum, are devoid of their gaseous and dusty phases of the ISM. Our models of galaxy evolution that are tailored to predict the effects of the cluster environment indicate that the ram pressure exerted by the dense intracluster medium on galaxies moving at high velocity within the cluster is able to remove their gaseous component of the ISM. The lack of gas induces a mild and gradual transformation of star-forming systems that have recently entered the cluster into quiescent red objects. The process is particularly efficient in dwarf systems that are easily perturbed because of their shallow potential well. Here, the migration from the blue cloud to the red sequence is very rapid (∼1 Gyr). This timescale is comparable to the time needed by a galaxy moving at ∼1000 km s^{-1}, the typical velocity dispersion of the cluster, to travel from the periphery to the cluster core and thus it explains the observed steep increase of the red-to-blue dwarf

galaxy fraction observed towards the core of Virgo. This mild process does not perturb the kinematic properties of the transformed galaxies that indeed conserve rotation curves similar to those of their star-forming analogues (Toloba et al. 2011, 2014). The distribution of dwarf red galaxies in the velocity space indicates that they recently entered the cluster. These freshly transformed objects can thus be at the origin of the faint end of the red sequence.

We can thus conclude that the most massive early-type galaxies in Virgo ($M_{\rm star} \gtrsim 10^{11}\ M_{\odot}$) are formed through major merging events that occurred far in the past. The fraction of objects in the red sequence formed through a major merging event, which have been identified thanks to their kinematic properties (slow rotators), rapidly decreases with decreasing stellar mass. These objects were probably formed during the assembly of the cluster through the merging of smaller groups (pre-processing), or are the result of galaxy harassment that occurred in galaxies belonging to the cluster since its earliest phases. With decreasing stellar mass, the fraction of red galaxies formed after a ram pressure stripping event able to remove the gaseous component of late-type galaxies and quench their activity becomes dominant.

Our analysis also shows that starvation, which is modelled by stopping gas infall in cluster galaxies, has much smaller effects even in the assumption that the process has started ∼10 Gyr ago. This process thus cannot explain the quenching of the star-formation activity observed in Virgo cluster galaxies and, thus, is hardly at the origin of the red sequence.

Acknowledgements. This research has been financed by the French ANR grant VIRAGE. We wish to thank the GALEX Time Allocation Committee for the generous allocation of time devoted to this project. We thank teh referee for constructive comments. M.F. acknowledges support by the Science and Technology Facilities Council [grant number ST/L00075X/1]. This research has made use of the NASA/IPAC Extragalactic Database (NED) which is operated by the Jet Propulsion Laboratory, California Institute of Technology, under contract with the National Aeronautics and Space Administration and of the GOLDMine database (http://goldmine.mib.infn.it/). GALEX (Galaxy Evolution Explorer) is a NASA Small Explorer, launched in 2003 April. We gratefully acknowledge NASA support for construction, operation, and science analysis for the GALEX mission, developed in cooperation with the Centre National d'Etudes Spatiales of France and the Korean Ministry of Science and Technology. Funding for the SDSS and SDSS-II has been provided by the Alfred P. Sloan Foundation, the Participating Institutions, the National Science Foundation, the US Department of Energy, the National Aeronautics and Space Administration, the Japanese Monbukagakusho, the Max Planck Society, and the Higher Education Funding Council for England. The SDSS Web Site is http://www.sdss.org/. The SDSS is managed by the Astrophysical Research Consortium for the Participating Institutions. The Participating Institutions are the American Museum of Natural History, Astrophysical Institute Potsdam, University of Basel, University of Cambridge, Case Western Reserve University, University of Chicago, Drexel University, Fermilab, the Institute for Advanced Study, the Japan Participation Group, Johns Hopkins University, the Joint Institute for Nuclear Astrophysics, the Kavli Institute for Particle Astrophysics and Cosmology, the Korean Scientist Group, the Chinese Academy of Sciences (LAMOST), Los Alamos National Laboratory, the Max-Planck-Institute for Astronomy (MPIA), the Max-Planck-Institute for Astrophysics (MPA), New Mexico State University, Ohio State University, University of Pittsburgh, University of Portsmouth, Princeton University, the United States Naval Observatory, and the University of Washington. R.G. and M.P.H. are supported by NSF grant AST-0607007 and by a grant from the Brinson Foundation. L.C. acknowledges support under the Australian Research Council's Discovery Projects funding scheme (project number 130100664).

References

Abazajian, K. N., Adelman-McCarthy, J. K., Agüeros, M. A., et al. 2009, ApJS, 182, 543
Auld, R., Bianchi, S., Smith, M. W. L., et al. 2013, MNRAS, 428, 1880
Balogh, M. L., Navarro, J. F., & Morris, S. L. 2000, ApJ, 540, 113
Barnes, J. E. 1992, ApJ, 393, 484
Barnes, J. E., & Hernquist, L. 1996, ApJ, 471, 115
Bell, E. F., & de Jong, R. S. 2001, ApJ, 550, 212
Bell, E. F., McIntosh, D. H., Katz, N., & Weinberg, M. D. 2003, ApJS, 149, 289
Benson, A., Toloba, E., Mayer, L., Simon, J., & Guhathakurta, P. 2014, ApJ, in press
Bigiel, F., Leroy, A., Walter, F., et al. 2008, AJ, 136, 2846
Binggeli, B., Sandage, A., & Tammann, G. A. 1985, AJ, 90, 1681
Binggeli, B., Tammann, G. A., & Sandage, A. 1987, AJ, 94, 251
Binggeli, B., Sandage, A., & Tammann, G. A. 1988, ARA&A, 26, 509
Binggeli, B., Popescu, C. C., & Tammann, G. A. 1993, A&AS, 98, 275
Böhringer, H., Briel, U. G., Schwarz, R. A., et al. 1994, Nature, 368, 828
Boissier, S., & Prantzos, N. 2000, MNRAS, 312, 398
Boissier, S., Prantzos, N., Boselli, A., & Gavazzi, G. 2003, MNRAS, 346, 1215
Boselli, A. 2011, A Panchromatic View of Galaxies, by A. Boselli, Practical Approach Book (Berlin: Wiley-VCH)
Boselli, A., & Gavazzi, G. 2006, PASP, 118, 517
Boselli, A., & Gavazzi, G. 2009, A&A, 508, 201
Boselli, A., Gavazzi, G., Donas, J., & Scodeggio, M. 2001, AJ, 121, 753
Boselli, A., Gavazzi, G., & Sanvito, G. 2003a, A&A, 402, 37
Boselli, A., Sauvage, M., Lequeux, J., Donati, A., & Gavazzi, G. 2003b, A&A, 406, 867
Boselli, A., Cortese, L., Deharveng, J. M., et al. 2005, ApJ, 629, L29
Boselli, A., Boissier, S., Cortese, L., et al. 2006, ApJ, 651, 811
Boselli, A., Boissier, S., Cortese, L., & Gavazzi, G. 2008a, ApJ, 674, 742
Boselli, A., Boissier, S., Cortese, L., & Gavazzi, G. 2008b, A&A, 489, 1015
Boselli, A., Boissier, S., Cortese, L., et al. 2009, ApJ, 706, 1527
Boselli, A., Eales, S., Cortese, L., et al. 2010, PASP, 122, 261
Boselli, A., Boissier, S., Heinis, S., et al. 2011, A&A, 528, A107
Boselli, A., Cortese, L., Boquien, M., et al. 2014, A&A, 564, A67
Bundy, K., Scarlata, C., Carollo, C. M., et al. 2010, ApJ, 719, 1969
Bureau, M., Jeong, H., Yi, S. K., et al. 2011, MNRAS, 414, 1887
Cappellari, M. 2013, ApJ, 778, L2
Cappellari, M., Emsellem, E., Krajnović, D., et al. 2011a, MNRAS, 413, 813
Cappellari, M., Emsellem, E., Krajnović, D., et al. 2011b, MNRAS, 416, 1680
Cayatte, V., van Gorkom, J. H., Balkowski, C., & Kotanyi, C. 1990, AJ, 100, 604
Cen, R. 2014, ApJ, 781, 38
Cen, R., Pop, A. R., & Bachall, N. A. 2014, PNAS, in press
Ciesla, L., Boselli, A., Smith, M. W. L., et al. 2012, A&A, 543, A161
Ciesla, L., Boquien, M., Boselli, A., et al. 2014, A&A, 565, A128
Colless, M., & Dunn, A. M. 1996, ApJ, 458, 435
Conselice, C. J., Gallagher, J. S., III, & Wyse, R. F. G. 2001, ApJ, 559, 791
Cortese, L., & Hughes, T. M. 2009, MNRAS, 400, 1225
Cortese, L., Davies, J. I., Pohlen, M., et al. 2010, A&A, 518, L49
Cortese, L., Catinella, B., Boissier, S., Boselli, A., & Heinis, S. 2011, MNRAS, 415, 1797
Cortese, L., Boissier, S., Boselli, A., et al. 2012a, A&A, 544, A101
Cortese, L., Ciesla, L., Boselli, A., et al. 2012b, A&A, 540, A52
Courteau, S., Cappellari, M., de Jong, R. S., et al. 2014, Rev. Mod. Phys., 86, 47
Cowie, L. L., Songaila, A., Hu, E. M., & Cohen, J. G. 1996, AJ, 112, 839
Cucciati, O., Iovino, A., Marinoni, C., et al. 2006, A&A, 458, 39
Cucciati, O., Marinoni, C., Iovino, A., et al. 2010, A&A, 520, A42
Cybulski, R., Yun, M. S., Fazio, G. G., & Gutermuth, R. A. 2014, MNRAS, 439, 3564
Davies, J. I., Baes, M., Bendo, G. J., et al. 2010, A&A, 518, L48
Davies, J. I., Bianchi, S., Cortese, L., et al. 2012, MNRAS, 419, 3505
de Looze, I., Baes, M., Zibetti, S., et al. 2010, A&A, 518, L54
De Looze, I., Baes, M., Boselli, A., et al. 2013, MNRAS, 436, 1057
De Lucia, G. 2011, Environment and the Formation of Galaxies: 30 Years Later, 203
De Lucia, G., Poggianti, B. M., Aragón-Salamanca, A., et al. 2004, ApJ, 610, L77
De Lucia, G., Springel, V., White, S. D. M., Croton, D., & Kauffmann, G. 2006, MNRAS, 366, 499
De Lucia, G., Poggianti, B. M., Aragón-Salamanca, A., et al. 2007, MNRAS, 374, 809
De Lucia, G., Poggianti, B. M., Halliday, C., et al. 2009, MNRAS, 400, 68
D'Eugenio, F., Houghton, R. C. W., Davies, R. L., & Dalla Bontà, E. 2013, MNRAS, 429, 1258
de Vaucouleurs, G. 1961, ApJS, 6, 213
Dressler, A. 1980, ApJ, 236, 351
Dressler, A. 2004, Clusters of Galaxies: Probes of Cosmological Structure and Galaxy Evolution, 206
Dressler, A., Oemler, A., Jr., Couch, W. J., et al. 1997, ApJ, 490, 577
Dressler, A., Smail, I., Poggianti, B. M., et al. 1999, ApJS, 122, 51
Dressler, A., Oemler, A., Jr., Poggianti, B. M., et al. 2013, ApJ, 770, 62
Elbaz, D., Daddi, E., Le Borgne, D., et al. 2007, A&A, 468, 33
Emsellem, E., Cappellari, M., Krajnović, D., et al. 2011, MNRAS, 414, 888
Ferrarese, L., Côté, P., Cuillandre, J.-C., et al. 2012, ApJS, 200, 4
Finn, R. A., Zaritsky, D., McCarthy, D. W., Jr., et al. 2005, ApJ, 630, 206

Fitzpatrick, E. L., & Massa, D. 2007, ApJ, 663, 320
Fontanot, F., De Lucia, G., Monaco, P., Somerville, R. S., & Santini, P. 2009, MNRAS, 397, 1776
Ftaclas, C., Struble, M. F., & Fanelli, M. N. 1984, ApJ, 282, 19
Fumagalli, M., & Gavazzi, G. 2008, A&A, 490, 571
Fumagalli, M., Krumholz, M. R., Prochaska, J. X., Gavazzi, G., & Boselli, A. 2009, ApJ, 697, 1811
Galardo, V. 2010, Ph.D. Thesis, University of Milano
Gavazzi, G., Pierini, D., & Boselli, A. 1996, A&A, 312, 397
Gavazzi, G., Boselli, A., Scodeggio, M., Pierini, D., & Belsole, E. 1999, MNRAS, 304, 595
Gavazzi, G., Boselli, A., Donati, A., Franzetti, P., & Scodeggio, M. 2003, A&A, 400, 451
Gavazzi, G., Fumagalli, M., Cucciati, O., & Boselli, A. 2010, A&A, 517, A73
Gavazzi, G., Fumagalli, M., Fossati, M., et al. 2013a, A&A, 553, A89
Gavazzi, G., Savorgnan, G., Fossati, M., et al. 2013b, A&A, 553, A90
Gerke, B. F., Newman, J. A., Davis, M., et al. 2005, ApJ, 625, 6
Gilbank, D. G., & Balogh, M. L. 2008, MNRAS, 385, L116
Gil de Paz, A., Boissier, S., Madore, B. F., et al. 2007, ApJS, 173, 185
Giovanelli, R., Haynes, M. P., Kent, B. R., et al. 2005, AJ, 130, 2598
Grossetti, F. 2010, Ph.D. Thesis, University of Milano
Gunn, J. E., & Gott, J. R., III 1972, ApJ, 176, 1
Haines, C. P., La Barbera, F., Mercurio, A., Merluzzi, P., & Busarello, G. 2006a, ApJ, 647, L21
Haines, C. P., Merluzzi, P., Mercurio, A., et al. 2006b, MNRAS, 371, 55
Hao, C.-N., Kennicutt, R. C., Johnson, B. D., et al. 2011, ApJ, 741, 124
Haynes, M. P., & Giovanelli, R. 1984, AJ, 89, 758
Haynes, M. P., Giovanelli, R., Martin, A. M., et al. 2011, AJ, 142, 170
Hoffman, G. L., Helou, G., Salpeter, E. E., & Lewis, B. M. 1989, ApJ, 339, 812
Houghton, R. C. W., Davies, R. L., D'Eugenio, F., et al. 2013, MNRAS, 436, 19
Hughes, T. M., & Cortese, L. 2009, MNRAS, 396, L41
Jaffé, Y. L., Aragón-Salamanca, A., De Lucia, G., et al. 2011, MNRAS, 410, 280
Jarrett, T. H., Masci, F., Tsai, C. W., et al. 2013, AJ, 145, 6
Kennicutt, R. C., Jr. 1998a, ARA&A, 36, 189
Kennicutt, R. C., Jr. 1998b, ApJ, 498, 541
Khochfar, S., Emsellem, E., Serra, P., et al. 2011, MNRAS, 417, 845
Kodama, T., Balogh, M. L., Smail, I., Bower, R. G., & Nakata, F. 2004, MNRAS, 354, 1103
Larson, R. B., Tinsley, B. M., & Caldwell, C. N. 1980, ApJ, 237, 692
Marinoni, C., Davis, M., Newman, J. A., & Coil, A. L. 2002, ApJ, 580, 122
Martin, D. C., Wyder, T. K., Schiminovich, D., et al. 2007, ApJS, 173, 342
Mastropietro, C., Moore, B., Mayer, L., et al. 2005, MNRAS, 364, 607
McLaughlin, D. E. 1999, ApJ, 512, L9
Mei, S., Blakeslee, J. P., Côté, P., et al. 2007, ApJ, 655, 144
Mo, H. J., Mao, S., & White, S. D. M. 1998, MNRAS, 295, 319
Moore, B., Lake, G., & Katz, N. 1998, ApJ, 495, 139
Muñoz-Mateos, J. C., Boissier, S., Gil de Paz, A., et al. 2011, ApJ, 731, 10
O'Connell, R. W. 1999, ARA&A, 37, 603
Platen, E., van de Weygaert, R., Jones, B. J. T., Vegter, G., & Calvo, M. A. A. 2011, MNRAS, 416, 2494
Poggianti, B. M., Bridges, T. J., Komiyama, Y., et al. 2004, ApJ, 601, 197
Quintero, A. D., Hogg, D. W., Blanton, M. R., et al. 2004, ApJ, 602, 190
Rines, K., Geller, M. J., Kurtz, M. J., & Diaferio, A. 2003, AJ, 126, 2152
Roediger, E., & Brüggen, M. 2007, MNRAS, 380, 1399
Schindler, S., Binggeli, B., & Böhringer, H. 1999, A&A, 343, 420
Schlegel, D. J., Finkbeiner, D. P., & Davis, M. 1998, ApJ, 500, 525
Schmidt, M. 1959, ApJ, 129, 243
Scott, T. C., Cortese, L., Brinks, E., et al. 2012, MNRAS, 419, L19
Scott, N., Davies, R. L, Houghton, R. C., et al. 2014, MNRAS, 441, 274
Scoville, N., Arnouts, S., Aussel, H., et al. 2013, ApJS, 206, 3
Stott, J. P., Smail, I., Edge, A. C., et al. 2007, ApJ, 661, 95
Stott, J. P., Pimbblet, K. A., Edge, A. C., Smith, G. P., & Wardlow, J. L. 2009, MNRAS, 394, 2098
Sun, M., Donahue, M., Roediger, E., et al. 2010, ApJ, 708, 946
Toloba, E., Boselli, A., Gorgas, J., et al. 2009, ApJ, 707, L17
Toloba, E., Boselli, A., Cenarro, A. J., et al. 2011, A&A, 526, A114
Toloba, E., Boselli, A., Peletier, R. F., et al. 2012, A&A, 548, A78
Toloba, E., Guhathakurta, P., Boselli, A., et al. 2014, ApJ, submitted
Tonnesen, S., & Bryan, G. L. 2009, ApJ, 694, 789
Treu, T., Ellis, R. S., Kneib, J.-P., et al. 2003, ApJ, 591, 53
van Haarlem, M. P., Cayon, L., Gutierrez de La Cruz, C., Martinez-Gonzalez, E., & Rebolo, R. 1993, MNRAS, 264, 71
Vollmer, B., Cayatte, V., Balkowski, C., & Duschl, W. J. 2001, ApJ, 561, 708
Voyer, E., Boselli, A., Boissier, S., et al. 2014, A&A, 569, A124
Whitmore, B. C., Gilmore, D. M., & Jones, C. 1993, ApJ, 407, 489
Wilman, D. J., & Erwin, P. 2012, ApJ, 746, 160
Wilman, D. J., Oemler, A., Jr., Mulchaey, J. S., et al. 2009, ApJ, 692, 298
Wright, E. L., Eisenhardt, P. R. M., Mainzer, A. K., et al. 2010, AJ, 140, 1868
Wyder, T. K., Martin, D. C., Schiminovich, D., et al. 2007, ApJS, 173, 293
Yagi, M., Yoshida, M., Komiyama, Y., et al. 2010, AJ, 140, 1814
Zibetti, S., Charlot, S., & Rix, H.-W. 2009, MNRAS, 400, 1181
Zwicky, F., Herzog, E., Wild, P., Karpowicz, M., & Kowal, C. T. 1961–1968, Pasadena: California Institute of Technology (CIT)

Pages 22 to 25 are available in the electronic edition of the journal at http://www.aanda.org

Appendix A: The WISE data

The NASA's Wide-field Infrared Survey Explorer (WISE, Wright et al. 2010) is a 40 cm space telescope with a field of view of 47′. The WISE satellite made an all sky survey in four photometric bands in the near- and mid-infrared domain (3.6, 4.5, 12, and 22 μm). The survey has been done by mapping the sky with 8.8 s exposures with an average twelve exposures per position, which allowed us to reach a point source sensitivity better than 4 mJy (5σ) at the ecliptic and significantly better at the ecliptic poles because of the longer exposures. The angular resolution at 22 μm is 12 arcsec, while the pixel size of the co-added images is 1.375″. Recently completed, the survey provides the community with fully reduced images that can be used to extract fluxes for all kinds of sources. Flux extraction within appropriate apertures is indeed required for the galaxies analysed in this work because of their extended nature. Flux densities provided by the WISE pipeline are generally underestimated in extended sources since the pipeline is optimised for point-like sources. For the purpose of this work, we retrieved the images of the whole Virgo cluster region in the 22 μm $W4$ band from the WISE Science Archive[8]. This band is close to the 25 μm IRAS and 24 μm *Spitzer* bands and can be easily used after simple corrections to quantify the attenuation in the FUV and NUV bands of GALEX using the prescription of Hao et al. (2011).

Fluxes have been extracted using exactly the same procedure adopted in Voyer et al. (2014) for the UV fluxes. Aperture photometry, indicated for extended sources such as those analysed in this work, has been done using the DS9/Funtools program *Funcnts*. This tool requires the use of different apertures: one centred on the emitting source encompassing the total emission and the others on the surrounding regions to estimate the sky contribution to the emission. For this purpose, we used exactly the same apertures on both the source and the sky as determined on the UV images by Voyer et al. (2014). These apertures were manually defined to include the total galaxy emission (elliptical aperture) and to avoid other emitting sources in the sky. We choose to use the same apertures as those used in the UV bands for several reasons. First of all, to avoid aperture effects in the extinction correction, the UV and infrared emitting flux must come from the same emitting regions. The shape of the on-source elliptical aperture (size and orientation) has been determined on the UV images of these extended sources to fully include the galaxy emission. Given the similar mid-infrared and UV morphology of galaxies, the same aperture is also well adapted in the 22 μm band. The on-source aperture is sufficiently large enough to encompass the total mid-infrared emission, which might be slightly more extended than the UV emission because of the higher resolution of GALEX (~5 arcsec). The sky regions have been selected on the UV images to avoid contaminating sources, such as background galaxies, nearby companions, or stars, which are rare in the UV bands at high Galactic latitudes. With the exception of stars, whose contribution in the WISE spectral domain under study is negligible, the nature of the possible emitting sources in the 22 μm band is similar to that of the UV sources. Both UV and mid-infrared images can be also contaminated by a low surface brightness, diffuse emission of Galactic cirri. The position of the sky regions around the target galaxy allows an accurate determination of the sky emission, thus minimising any systematic effect related to this diffuse component.

The DS9/Funtools program *Funcnts* has been run on all the extended UV detected sources catalogued in Voyer et al. (2014) (1771 objects). Counts have been transformed into flux densities (in Jy) using the prescriptions given in Wright et al. (2010) and in the Explanatory Supplement WISE Preliminary Data Release Products consistently with Ciesla et al. (2014), by using 5.2269×10^{-5} Jy/DN. We also applied, as suggested by Jarrett et al. (2013), an aperture correction of −0.03 mag to account for the WISE absolute photometric calibration method by using PSF profile fitting. We also applied a second correction to account for a systematic difference in the calibrating "red" stars and "blue" galaxies. Jarrett et al. (2013) quantified this error for star-forming galaxies with a spectrum rising as $S(\nu) \sim \nu^{-2}$ and removed it by applying a systematic correction of 0.92 in the 22 μm band. We did not apply this correction to quiescent, early-type galaxies since the emission might still be dominated by the Rayleigh-Jeans tails of the stellar atmosphere of M type stars in this band. We did not apply any further colour correction, since it is negligible in the $W4$ WISE band (~1%; Jarrett et al. 2013). Combined with calibration uncertainties (~1.5%), the photometric uncertainty due to aperture and colour corrections on the $W4$ band should be of the order of ~5%. This, however, does not include the uncertainty on the total flux estimate, which is generally dominated by the uncertainty on the determination of the sky background in extended sources (Boselli et al. 2003b; Ciesla et al. 2012). The total uncertainty on the measure of the flux density is thus given by the quadratic sum of the calibration uncertainty $err_{\rm WISE}$, on the uncertainty of the large scale sky fluctuations $err_{\rm sky}$, and on the pixel per pixel uncertainty $err_{\rm pix}$ which might be partly correlated (Boselli et al. 2003b; Ciesla et al. 2012). Consistently with Boselli et al. (2003b) and Voyer et al. (2014), we calculate the uncertainty on the sky $err_{\rm sky}$ and on the pixel per pixel $err_{\rm pix}$ in ~10 square sky regions with randomly selected large sizes surrounding each target. These uncertainties are defined as:

$$err_{\rm sky} = N_{\rm pix} STD\,[\langle b_1\rangle \ldots \langle b_n\rangle] \quad (A.1)$$

$$err_{\rm pix} = \sqrt{N_{\rm pix}}\,\langle STD[b_1] \ldots STD[b_n]\rangle, \quad (A.2)$$

where $N_{\rm pix}$ is the number of pixels in the galaxy aperture, $STD[b_n]$ is the standard deviation of the values of all pixels in sky box n, and $\langle b_n\rangle$ is the average of all pixels in sky box n (Voyer et al. 2014). The total uncertainty on the extracted flux is then given by

$$err_{\rm tot} = \sqrt{err_{\rm sky}^2 + err_{\rm pix}^2} \quad (A.3)$$

to which the calibration uncertainty $err_{\rm WISE}$ should be added for estimating the total photometric uncertainty on the data. Given that $err_{\rm sky}$ and $err_{\rm pix}$ are the dominant source of error, we consider all galaxies with $S_{22\,\mu{\rm m}}/err_{\rm tot} > 1$ here as detections. As in Boselli et al. (2003b) for undetected galaxies, we estimate an upper limit defined as

$$S_{22\,\mu{\rm m}}(up.lim.) = 2 \times \sqrt{err_{\rm sky}^2 + err_{\rm pix}^2}. \quad (A.4)$$

The WISE 22 μm flux densities of all the UV extended sources and their uncertainties are listed in Table A.1, which is arranged as follow:

- Column 1: Galaxy name, from NED.
- Columns 2 and 3: right ascension (J2000) and declination of the aperture used to extract the 22 μm WISE flux density.

[8] http://wise2.ipac.caltech.edu/docs/release/allsky/

Table A.1. Example of WISE data.

Name	$RA(J2000)_{ap}$	Dec_{ap}	a	b	PA	flag	$S_{22\,\mu m}$
	deg	deg	$''$	$''$	deg		mJy
(1)	(2)	(3)	(4)	(5)	(6)	(7)	(8)
CGCG-013019A	179.60542	0.70688	19.7	10.1	96	0	0.7
CGCG-013019B	179.60883	0.71311	15.0	8.3	60	0	0.3
CGCG-013019C	179.61542	0.71789	19.0	12.0	149	1	1.3 ± 0.4
CGCG-013034	180.07496	0.29497	30.8	12.6	102	1	22.3 ± 0.6
CGCG-013035	180.09963	0.49067	20.0	12.0	264	1	2.4 ± 0.4
CGCG-013036	180.27079	0.11375	25.0	10.0	225	1	1.6 ± 0.5
CGCG-013042	180.52258	1.52589	17.9	17.0	199	1	1.3 ± 0.6
CGCG-013045	180.67788	1.95219	28.1	13.8	231	1	2.8 ± 0.4
CGCG-013046	180.67462	1.97880	90.0	66.6	0	1	658.3 ± 6.4
CGCG-013049	180.80517	1.95092	25.0	20.0	151	1	2.3 ± 0.7
CGCG-013050	180.87304	1.22936	27.9	17.0	180	1	1.9 ± 0.7
CGCG-013051	180.90675	2.04692	20.0	13.0	187	0	0.8
CGCG-013054	180.99783	1.41075	23.0	19.0	102	1	10.3 ± 0.7
CGCG-013055	181.02496	1.84697	13.0	30.0	9	1	1.1 ± 0.7
CGCG-013056	181.04058	1.82594	33.2	16.6	133	1	8.2 ± 1.0
CGCG-013057	181.08333	1.56758	70.8	15.6	189	1	29.1 ± 1.1
CGCG-013058	181.07917	1.84839	19.0	11.5	252	0	0.7
CGCG-013059	181.11038	1.89660	56.7	43.9	20	1	11.7 ± 2.2
CGCG-013060	181.14192	1.73822	16.1	11.6	199	0	0.5
CGCG-013061	181.14179	1.80161	35.0	15.0	249	0	1.1
CGCG-013063	181.15829	1.78580	36.0	25.2	100	1	19.8 ± 0.7
CGCG-013064	181.15762	2.07253	45.0	23.1	216	1	7.0 ± 1.3
CGCG-013069	181.33979	2.08631	21.5	14.6	102	0	1.3
CGCG-013072	181.41971	1.57506	37.2	10.4	187	0	1.3
CGCG-013073	181.41942	1.59350	17.0	13.0	168	0	0.6
CGCG-013076	181.63150	1.61656	20.0	18.0	120	1	6.8 ± 0.5
CGCG-013079	181.90867	1.57419	30.4	14.0	148	0	1.6
CGCG-013080	181.99996	1.39594	25.0	20.0	210	1	2.8 ± 0.6
CGCG-013083	182.09800	0.11028	19.6	15.7	247	1	6.3 ± 0.5
CGCG-013084	182.13046	0.13650	28.2	15.8	200	1	8.9 ± 0.8
CGCG-013085	182.13021	1.90958	45.0	11.0	216	1	7.8 ± 1.2
CGCG-013087	182.36933	0.53325	19.2	10.0	169	1	15.6 ± 0.4
CGCG-013089	182.47446	0.92850	42.0	21.0	148	1	34.0 ± 1.0
CGCG-013095	182.63588	0.67750	37.9	19.7	161	0	2.3
CGCG-013096	182.76692	0.97233	25.0	25.0	178	0	2.6
CGCG-013100	182.99771	1.35003	40.0	17.0	258	1	3.7 ± 1.5
CGCG-013104	183.21725	1.30000	114.0	33.0	235	0	27.0
CGCG-013105	183.42004	2.18769	22.0	19.0	230	0	4.3
CGCG-013110	183.68938	0.74353	50.0	15.0	143	1	14.7 ± 1.5
CGCG-013113	183.96875	0.40069	50.0	37.0	244	1	22.5 ± 4.6
CGCG-013116	184.01867	1.18042	25.0	19.0	134	1	34.5 ± 1.4

- Columns 4–6: major and minor axis radii (in arcsec) and position angle (measured in degrees from north clockwise) of the adopted aperture.
- Column 7: flag indicating whether a galaxy is detected (1) or undetected (0).
- Column 8: 22 μm WISE flux density and error err_{tot} as defined in Eq. (9) in mJy.

To check the quality of these WISE data, we compare them to those already available in the literature in similar photometric bands. We first use a compilation of 25 μm IRAS data taken from different sources in the literature, which is available for 119 galaxies of the sample (Boselli et al. 2010). The comparison of the two sets of data is shown in Fig. A.1. Figure A.1 shows that the WISE and IRAS sets of data are fairly consistent for flux densities $S_{IRAS}(25\,\mu m) \gtrsim 400$ mJy. Below this threshold, which roughly corresponds to the detection limit of IRAS in the 25 μm band, the WISE flux densities are systematically smaller than the IRAS one, thereby suggesting that these IRAS values are probably spurious detections. By comparing 24 μm MIPS *Spitzer* data to 22 μm WISE data for the HRS, Ciesla et al. (2014) found a systematic shift in the two sets of data of a factor 1.22 that they imputed to the slightly different spectral range covered by the two instruments. Figure A.1 shows that the same systematic shift can explain the observed difference in the IRAS and WISE data.

Figure A.2 shows the comparison of the 22 μm WISE flux densities determined in this work with those recently published by Ciesla et al. (2014) for the HRS galaxies in common (138 detected objects). Figure A.2 shows that our set of data is perfectly consistent with the one of Ciesla et al. (2014). The mean Ciesla et al. (2014) to this work flux density ratio $S_{HRS}/S_{T.W.}$ for the 138 detected galaxies in common is $S_{HRS}/S_{T.W.} = 1.01 \pm 0.63$. The dispersion significantly drops when we limit the comparison to late-type systems ($S_{HRS}/S_{T.W.} = 0.99 \pm 0.10$; 105 objects), which are the galaxies where the WISE data are crucial for an accurate dust extinction correction, while it is higher in early-type systems ($S_{HRS}/S_{T.W.} = 1.06 \pm 1.30$; 33 objects). This systematic difference in early-type galaxies, where the 22 μm WISE emission might still be dominated by the stellar emission and is thus limited to the innermost brightest regions,

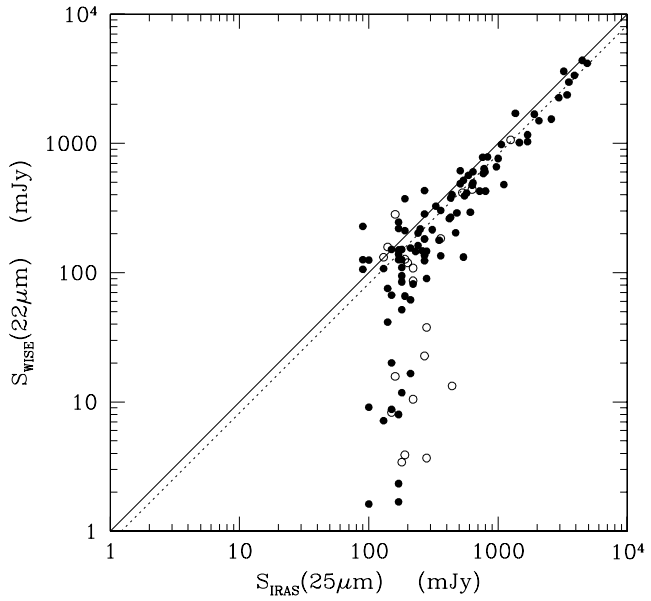

Fig. A.1. Comparison of the 22 μm WISE flux densities determined in this work with those measured at 25 μm by IRAS for 119 detected galaxies in common. The solid line shows the 1:1 relation, while the dotted line is the expected relation once the WISE data are corrected by a factor of 1.22, as indicated by Ciesla et al. (2014) to take the shift in the photometric bands into account. Filled dots indicates late-type galaxies, empty-symbols early-types.

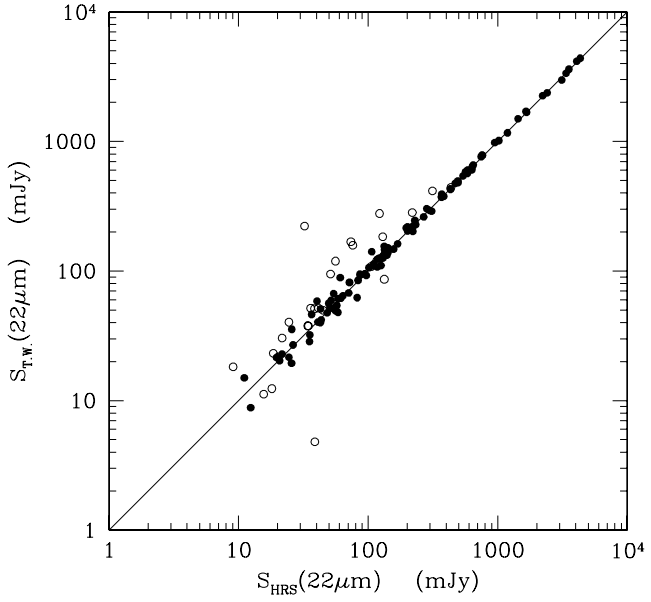

Fig. A.2. Comparison of the 22 μm WISE flux densities for 138 HRS galaxies included in our sample. Filled dots indicates late-type galaxies, empty-symbols early-types. The solid line shows the 1:1 relation.

is due to the reason that while here we keep the same aperture than the one used to integrate the UV emission, in Ciesla et al. (2014) the apertures are manually adapted to encompass the total infrared emission on the WISE images and thus minimise the uncertainties due to the sky fluctuations. The procedure adopted in Ciesla et al. (2014) for early-type systems, thus, should give more accurate results. We recall that the 22 μm flux densities of early-type galaxies are not used for the dust attenuation correction of the UV and optical photometric data. They are reported here just for completeness.

Table A.2. Cumulative and differential WISE detection rate.

Cumulative			
M_{star} range	All	E-S0a	Sa-Im-BCD
$M_\odot$	%	%	%
$M_{star} \geq 10^{10}$	82	68	98
$M_{star} \geq 10^{9}$	73	53	90
$M_{star} \geq 10^{8}$	56	38	80
$M_{star} \geq 10^{7}$	48	30	70
Differential			
M_{star} range	All	E-S0a	Sa-Im-BCD
$M_\odot$	%	%	%
$10^{9} \leq M_{star} \leq 10^{10}$	68	42	89
$10^{8} \leq M_{star} \leq 10^{9}$	41	27	65
$10^{7} \leq M_{star} \leq 10^{8}$	20	6	38

Table A.2 gives the cumulative and differential detection rate in the 22 μm band in different bins of stellar mass for the whole sample of Virgo galaxies and separately for early- and late-type galaxies. The overall detection rate of late-type galaxies, where 22 μm flux densities are necessary for an accurate extinction correction, is fairly good (~70%) although it drops to 38% in the lowest stellar mass bin.

Appendix B: The stellar mass determination

The standard recipes such as those proposed by Bell & de Jong (2001), Bell et al. (2003), Zibetti et al. (2009), and Boselli et al. (2009) to estimate the stellar mass of galaxies using a combination of a stellar luminosity with an optical or near-infrared colour index have been calibrated using different population synthesis models and initial mass functions (IMF) and assume different realistic star-formation histories. These star-formation histories are generally assumed to reproduce the smooth evolution of unperturbed objects of different luminosity and morphological type. They are thus not ideally defined to reproduce the evolution of strongly perturbed galaxies in high-density environments, such as those analysed in this work. Indeed, the removal of the atomic and molecular gas content for a ram pressure stripping event is very rapid in cluster galaxies and is thus able to quench the activity of star formation on very short timescales. Thus, the standard recipes for determining the total stellar mass proposed in the literature might not be optimised for perturbed galaxies, such as those analysed in this work. Their adoption can induce systematic effects in the analysed sample. To quantify these effects, we plot the relationship between the i-band mass-to-light ratio and the $g - i$ colour index for galaxies of different stellar mass in Fig. B.1 as predicted by our multizone chemo-spectrophotometric models of galaxy evolution and those predicted by the prescription of Zibetti et al. (2009). Figure B.1 shows a tight correlation between the two variables for unperturbed galaxies using either our evolutionary models or the predictions of Zibetti et al. (2009), although this last gives a steeper relation. The observed difference in the two relations for unperturbed galaxies comes from the use of different population synthesis models, the adoption of different IMF, and star-formation histories of the target galaxies (e.g. Courteau et al. 2014). In this comparison, the main difference is that our model concerns disk galaxies while Zibetti et al. (2009) is a fit to the M/L-colour diagram obtained for a set of models which include a very large variety of star-formation histories (not only adapted to star forming galaxies). The Zibetti et al. fit is thus an average of "active"

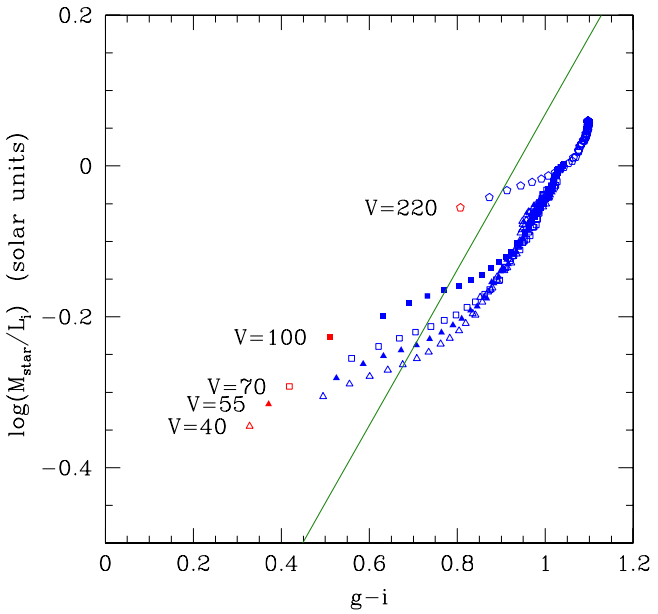

Fig. B.1. Relationship between the stellar mass-to-*i*-band luminosity ratio and the $g-i$ colour index, as predicted by the calibration of Zibetti et al. (2009) (green solid line), and our models of galaxy evolution for unperturbed galaxies of different rotational velocity and fixed spin parameter ($\lambda = 0.05$; red open symbols), as well as for galaxies undergoing a ram pressure stripping event (blue symbols).

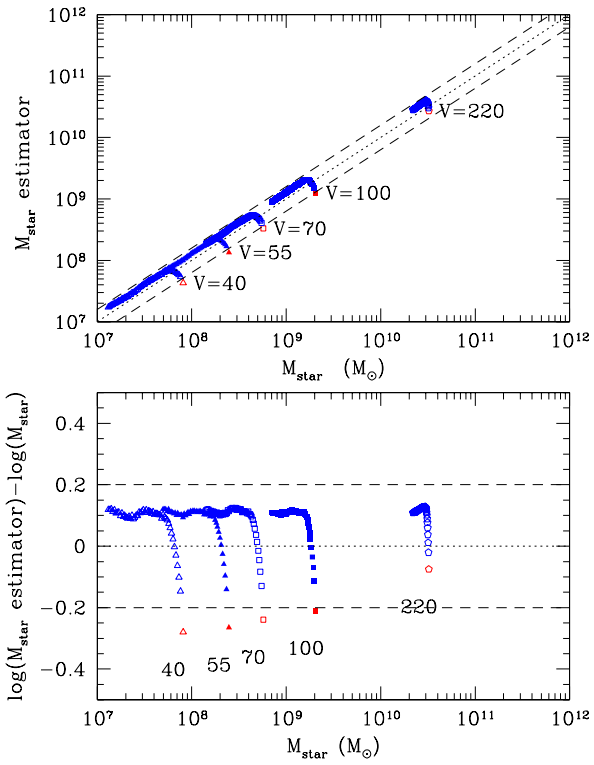

Fig. B.2. *Upper panel*: relationship between the stellar mass estimated using the Zibetti et al. (2009) mass-to-light colour dependent calibration and the real stellar mass of galaxies in our models of galaxy evolution for unperturbed (red symbols) and ram pressure stripped objects (blue symbols). The dotted line gives the 1:1 relation, while the dashed lines shows a variation of 0.2 dex (this value is typical of the global uncertainties affecting mass determinations due to the choice of the IMF). *Lower panel*: logarithmic difference between the stellar mass estimated using the Zibetti et al. (2009) mass-to-light colour dependent calibration and the stellar mass from our models for unperturbed (red symbols) and ram pressure stripped objects (blue symbols) is plotted vs. the stellar mass of the model galaxies.

galaxies (similar to our bluest models in the absence of interaction) and of "passive" galaxies (similar to our reddest models in which the interaction has reduced the star-formation activity).

Figure B.1 also shows that the relationship between $M_{\rm star}/L(i)$ and $g-i$ significantly changes in perturbed galaxies. This is obvious, since the colour of a galaxy significantly changes becoming redder once the galaxy has abruptly stopped its star-formation activity, as indeed indicated by our models (Boselli et al. 2006, 2008a). If the *i*-band luminosity is barely affected after a ram pressure stripping event, the colour can significantly change on relatively short timescales. The adoption of a unique relation using standard recipes based on stellar luminosities and colours might thus induce strong systematic biases in the stellar mass determination. It would be more appropriate to use a standard spectral energy distribution fitting code, provided that realistic truncated star-formation histories, such as those observed in our sample can be easily reproduced. To effectively constrain the star-formation history of galaxies, however, a full coverage of the UV-to-far-infrared spectral energy distribution is necessary. This, unfortunately, is still quite prohibitive in the nearby universe for samples, such as the one analysed in this work, which span a wide range in luminosity (from giant to dwarfs) and morphological type (from ellipticals to irregulars). Furthermore, the star-formation history of the target galaxies, which is the topic of the present work, is an unknown variable, while not all fitting codes are tuned for such a purpose[9]. We thus decided to estimate stellar masses using a standard recipe and to quantify the uncertainty and any possible systematic effects on the derived $M_{\rm star}$ by comparing the prediction of our evolutionary models with the mass-to-light ratio vs. colour relations proposed in the literature. This is done in Fig. B.2, where the *i*-band stellar mass-to-light ratio predicted by the Zibetti et al. (2009) prescription is plotted vs. the optical $g-i$ colour and compared to the predictions of our multizone chemo-spectrophotometric models.

In unperturbed galaxies, Fig. B.2 shows that the prescription of Zibetti et al. (2009) compared to our models underpredicts the stellar mass of galaxies by a factor of ~0.3–0.1 dex (larger values are for dwarf systems), while it overpredicts the mass in perturbed, gas deficient objects where the star-formation activity is rapidly quenched after a ram pressure stripping event. In these objects, however, the overprediction is just by ~0.1 dex irrespective of stellar mass. Although important, Fig. B.2 shows that the systematic effect in the determination of the stellar mass using the recipe of Zibetti et al. (2009) is relatively small compared to the dynamic range in the stellar mass sampled in this work. We thus decided to use the Zibetti et al. (2009) relation, since it gives an "average" value for unperturbed and perturbed objects. Figure B.2 can be used to quantify the systematic effect on stellar mass for different galaxies.

[9] These codes generally use parametrised star-formation histories not always defined to reproduce the abrupt truncation observed in cluster galaxies.